ORGANIC REDOX CATALYSTS FOR OXYGEN ELECTROREDUCTION TO

HYDROGEN PEROXIDE:

AN APPLICATION TO DRINKING WATER TREATMENT

by

Yu-Sheng Andrew Wang

B.A.Sc., The University of British Columbia, 2009

A THESIS SUBMITTED IN PARTIAL FULFILLMENT OF

THE REQUIREMENTS FOR THE DEGREE OF

MASTER OF APPLIED SCIENCE

in

THE FACULTY OF GRADUATE STUDIES

(Chemical and Biological Engineering)

THE UNIVERSITY OF BRITISH COLUMBIA

(Vancouver)

April 2012

Abstract

Conventional H_2O_2 production entails an energy and capital intensive Riedl-Pfleiderer process, which is advantageous based on the economy of scale, yet it generates large amounts of toxic waste. The electrochemical synthesis of H_2O_2 can potentially emerge in small and remote applications, where the transportation and handling of concentrated H_2O_2 can be avoided. The commercial Dow-Huron electrolysis cell has shown some success in the pulp and paper industry. However, its highly caustic product (pH > 13) may limit its wide-spread application. Electrocatalytically, the two electron reduction of O_2 in near neutral or acidic media has proven challenging. In addition to cobalt macrocycle-based catalysts, quinone-based redox catalysts have also been successfully demonstrated as viable electrocatalysts. The present work reports the synthesis of a novel riboflavinyl-anthraquinone (RF-AQ) compound which showed redox catalytic activity for O_2 reduction to H_2O_2. Cyclic voltammetry with a rotating ring-disk electrode assembly was employed to characterize the catalyst. Chromoamperommetry experiments in a batch electrolysis cell were performed, using 0.5 M H_2SO_4 saturated with O_2, up to 24 hours at 21^oC and $1bar_{abs}$ to demonstrate the longer term H_2O_2 synthesis. Modifications of the Vulcan XC72 by RF-AQ adsorption increased the onset potential of the O_2 reduction reaction by up to 50 mV compared to Vulcan XC72 alone. A H_2O_2 selectivity of up to $85 \pm 5\%$ was observed for the RF-AQ catalyst. Chronoamperommetry, via constant potential control at 0.1V vs. RHE, with the 10 wt% RF-AQ catalyst (composite loading of 2.5 mg cm^{-2}) generated H_2O_2 with an initial rate (in two hours) of 21 $\mu mol\ hr^{-1}\ cm^{-2}$ (normalized by the electrode geometric area) and accumulated up to 425 $\mu mol\ cm^{-2}$ (normalized by electrode area) in 24 hours with a current density of about 1.3 mA cm^{-2} at $70 \pm 5\%$ current efficiency. While the unmodified Vulcan

XC72, with a similar catalyst weight loading and the same cathode potential, generated H_2O_2 with an initial rate of 6 μmol hr^{-1} cm^{-2} (normalized by electrode area) and accumulated only up to 140 μmol cm^{-2} (normalized by electrode area) in 24 hours with a current density of about 0.55 mA cm^{-2} at $55 \pm 5\%$ current efficiency.

Preface

All literature review, design of the experimental setup, experimental data collection and analysis were conducted by Andrew Wang, under the supervision of Prof. Elod Gyenge, Prof. David Wilkinson and Dr. Arman Bonakdarpour. The material covered in *Chapter 4* was published in:

A. Wang, A. Bonakdarpour, D.P. Wilkinson, E. Gyenge, Novel organic redox catalyst for the electroreduction of oxygen to hydrogen peroxide, Electrochimica Acta, 2012. 66 (1): p. 222-229.

The thesis manuscript was reviewed by the M.A.Sc. Committee, which included Dr. Elod Gyenge, Dr. David Wilkinson, Dr. Colin Oloman, and Dr. Jiujun Zhang.

Table of Contents

List of Tables

List of Figures

List of Abbreviations

ABS	Absorbance
AOP	Advanced oxidation process
AQ	Anthraquinone
CAQ	Anthraquinone-2-carboxylic acid
CV	Cyclic voltammetry
DAAQ	1,2-diamino-anthraquinone
DBP	Disinfection byproduct
DI	Deionized
EAQ	2-ethyl-anthraquinone
FTIR	Fourier transform infrared
GC	Glassy carbon
IR	Infrared
MSE	Mercury-mercurous sulphate reference electrode
NOM	Natural organic matter
OCV	Open-circuit potential
PEM	Polymer electrolyte membrane
PQ	Phenanthrenequinone
PTFE	Poly-tetra-flouro-ehtylene
py	Pyridine
RF	Riboflavin
RF-AQ	Riboflavinyl-anthraquinone-2-carboxylate ester
RHE	Reversible hydrogen electrode
RRDE	Rotating ring-disk electrode
RVC	Reticulated vitreous carbon
SHE	Standard hydrogen electrode
UV	Ultaviolet
VOC	Volatile organic compound

List of Symbols

a_i^j	Activity of species i in phase j	-
A	Electrode area	cm^2
α	Electron transfer symmetry coefficient	-
β	$\exp\left(-\Delta\overline{G}_1^{\,0}/RT\right)$	-
C_i^j	Concentration of species i in phase j	$mole\ cm^{-3}$
D_{i/H_2O}	Diffusion coefficient of species i in water	$cm^2\ s^{-1}$
E^0	Standard electrode potential	V
$\Delta E_{p,1/2}$	Half wave peak separation	V
F	Fardaday's constant	$96485\ C\ mole^{-1}$
g	Frumkin isotherm correction factor	$J\ cm^2\ mole^{-2}$
$\Delta\overline{G}_1^{\,0}$	Standard free energy of adsorption	$J\ mole^{-1}$
h	Planck's constant	J s
ΔH^0	Change in standard enthalpy	$J\ mole^{-1}$
I	Electrical current	mA
i, i_F, i_k, i_{dl}	Electrical current density; subscript: Faradaic, kinetic limiting, and diffusion limiting	$mA\ cm^{-2}$
k^0, k_f	Intrinsic standard and forward reaction rate constant	s^{-1}
k	Apparent reaction rate constant	$cm\ s^{-1}$
$k_{H_2O_2}$	Apparent reaction rate for H_2O_2 decomposition	$ppm_{wt}\ day^{-1}$
n	Number of electrons transferred	-
R	Gas constant	$8.31\ Jmole^{-1}K^{-1}$
Γ_i	Adsorption coverage of species i	$mole\ cm^{-2}$
Γ_{mon}	Monolayer adsorption coverage of species i	$mole\ cm^{-2}$
T	Temperature	K
t	Time	s
ν	Potential sweep rate	$V\ s^{-1}$
υ	kinematic viscosity	$cm^2\ s^{-1}$
$\overline{\mu}_1^{\,0}$	Standard electrochemical potential of species i	-
ω	Electrode rotation speed	s^{-1}

Acknowledgements

This research project would not have been possible without the support of many people. Many thanks to the Department of Chemical and Biological Engineering, staff and colleagues. I offer my deepest gratitude to my supervisors, Prof. Elöd Gyenge and Prof. David Wilkinson, for the superb supervision during the past two years. Gratitude also goes to Dr. Arman Bonakdarpour and Winton Li for the advice and assistance throughout this project. I sincerely appreciate and value the friendly atmosphere and insightful conversations I had enjoyed with colleagues working in CHBE 6.08 and 6.18.

Many thanks to the IRC freenode Internet chemists from around the globe for laughing at my silly accidents in the lab, especially the thiocyanide incident. Big thanks to my friend Mohammad El-Gamacy from the Faculty of Pharmacy at Ain Shams University, Egypt, for helping me use ChemBio Office to estimate the molecular volume of RF-AQ.

I express my gratitude to the NSERC Res'eauWaterNET strategic network for the financial support.

I would especially like to thank my 6-year old laptop as well as Microsoft Word processor for always working for me and never crashing during the writing of this thesis. The same cannot be said about Microsoft Excel. Grand appreciation goes to Mother Nature for the wonderful weather and the City of Vancouver for providing me with ample electricity.

Chapter 1: Introduction

Canada takes pride in hosting an abundance of freshwater, one of nature's most vital natural resources. About 7% of the global renewable freshwater is located throughout Canada [1]. It is therefore no surprise that much attention and public inquiry were directed towards water crises such as the 2000 *E. coli* outbreak in Walkerton, Ontario with a toll of 7 deaths and 2300 illnesses [2]. Much less attention, however, has been given to the small and rural communities throughout Canada, many of which are First Nations. As of November 2011, 131 First Nations communities were under drinking water advisories, and close to 100 of them had been under permanent (exceeding 6 months) boil water advisories [3]. One significant reason for long-term drinking water advisories is the public consensus in these small communities to lower or eliminate the chlorination disinfection process, primarily due to concerns about the effects of chlorination and the taste of chlorine treated water. Concerns with chlorination include disinfection byproducts – most pronouncedly trihalomethanes (THMs), carcinogens which could bioaccumulate in the human body [4]. The Res'eau Waternet research network was established in 2008 to address the issues of drinking water quality in small and rural communities, and identified advanced oxidation processes (AOPs) a viable technology to address the issues of permanent water advisories.

1.1 Advanced Oxidation Processes for Drinking Water Treatment

AOPs are capable of treating a wide range of common water borne pollutants such as natural organic matter (NOM), volatile organic compounds (VOCs), disinfection byproducts (DBPs), pesticides, drug residues, *E. coli*, and cryptosporidium [5]. The effectiveness of the treatment depends on the strength of the oxidant. Table 1.1 lists some oxidizing agents in the

order of their potential. The hydroxyl radical ranks amongst the top. In addition to its non-selective decomposition of organic contaminants, the ultimate $HO^{\bullet}$ disinfection byproducts are H_2O, CO_2 and inert salts, making the process environmentally friendly and the treated water practically taste-free.

Table 1.1 Oxidation potential of common species (modified from Parsons[4] with permission from Iwa Publishing)

Species	Standard Oxidation Potential at 298 K (V vs. SHE)
Flourine (F_2)	3.03
Hydroxyl radical ($HO^{\bullet}$)	2.80
Atomic oxygen (O)	2.42
Ozone (O_3)	2.07
Hydrogen peroxide (H_2O_2)	1.78
Perhydroxyl radical ($HOO^{\bullet}$)	1.70
Permanganate (MnO_4^{2-})	1.68
Hypobromous acid (HBrO)	1.59
Chlorine dioxide (ClO_2^-)	1.57
Hypochloric acid (HClO)	1.49
Chlorine (Cl_2)	1.36

In the AOP process, hydroxyl radicals can be directly generated from the photohomolysis of H_2O_2 by UV irradiation at a wavelength less than 254 nm, according to Eqn 1.1 [6]. Excess H_2O_2 can scavenge hydroxyl radicals (Eqn 1.2 – 1.4) and thus lower its effectiveness in the disinfection process. Typically 5 to 10 ppm of H_2O_2 is employed in the AOP process to mitigate this issue.

$$H_2O_2 + h\upsilon \rightarrow 2HO^{\bullet} \qquad (1.1)$$
$$HO^{\bullet} + H_2O_2 \rightarrow HO_2^{\bullet} + H_2O \qquad (1.2)$$
$$HO_2^{\bullet} + H_2O_2 \rightarrow HO^{\bullet} + H_2O + O_2 \qquad (1.3)$$
$$2HO_2^{\bullet} \rightarrow H_2O_2 + O_2 \qquad (1.4)$$
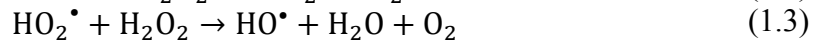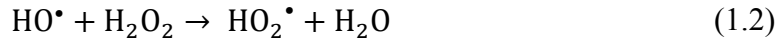
HO$^•$ may also be generated from ozone in a similar fashion. H_2O_2 is preferred because its homolysis is energetically favoured, and its storage is also simpler than O_3. H_2O_2 is totally miscible with water and stable in most aqueous solutions; whereas ozone has a solubility of just 1.05 g cm^{-3} [7]. From an energetic point of view, the O-O bond in H_2O_2 has a bond order of 1, while that in O_3 has a bond order of 1.5. Consequently it is much more efficient to break the O-O bond in H_2O_2 (bond energy 142 kJ mol^{-1}) compared to that in O_3 (bond energy 364 kJ mol^{-1}).

Table 1.2 compares decomposition reaction rate constants (using a pseudo-first order reaction rate model) of several common pollutants by O_3 and by HO$^•$. For a wide range of pollutants, HO$^•$ treatment can be over 10^9 times as effective as ozone. The decomposition reaction pathways for the pollutants are complex due to the many possible reactions, dependent on the oxidant concentration, pH, temperature, and presence of ions.

Table 1.2 Rate constants for ozone and hydroxyl radical treatments (adapted from Parsons[4] with permission from Iwa Publishing)

Organic pollutant	Decomposition rate constants at 298 K [M^{-1} s^{-1}]	
	O_3	HO$^•$
Benzene	2	7.8 x 10^9
Toluene	14	7.8 x 10^9
Chlorobenzene	0.75	4 x 10^9
Trichloroethylene	17	4 x 10^9
Tetrachloroethylene	< 0.1	1.7 x 10^9
n-Butanol	0.6	4.6 x 10^9
t-Butanol	0.03	0.4 x 10^9

The two major costs associated with the UV-H_2O_2 process are the electrical energy consumption and H_2O_2 consumption. The list price for 50% technical grade hydrogen peroxide is \$0.35 per lb, and the transportation cost is \$3.5 per mile freight [8]. Some

production plants in Canada are located at: Gibbons, Alberta; Becancour, Quebec; Maitland, Ontario; and Prince George, British Columbia. For small and remote water treatment facilities, it is neither economical nor safe to handle and store concentrated H_2O_2 on-site. H_2O_2 decomposition generates gaseous O_2 and intense heat (100.4 kJ mol^{-1}). Also, the vapour of 70 w% H_2O_2 can cause spontaneous ignition of combustible materials at room temperature. Its transportation also poses threats to infrastructure and personnel. A small scale onsite H_2O_2 generation process would eliminate these threats.
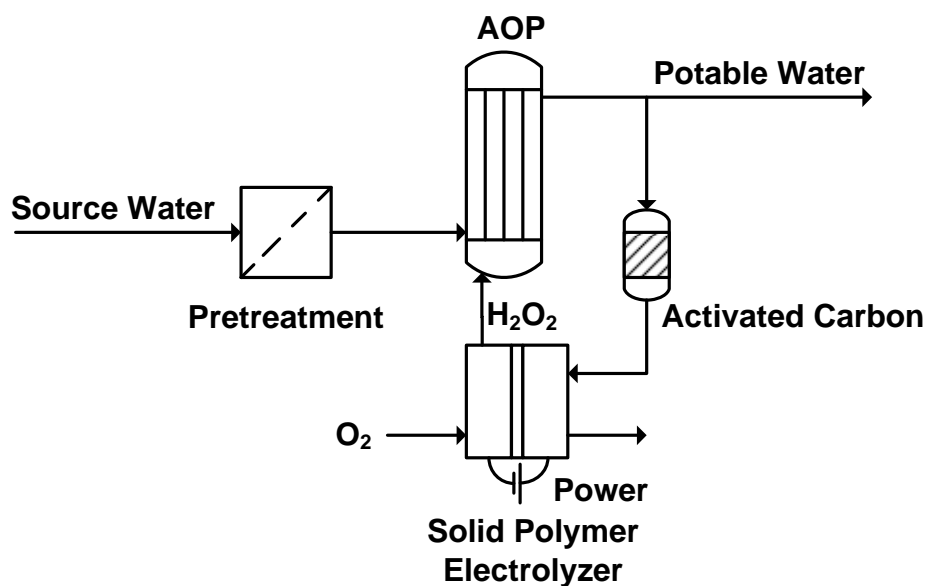
Figure 1.1 Simplified scheme of on-site electrochemical H_2O_2 synthesis for AOP process

A simplified scheme of an on-site electrochemical H_2O_2 synthesis process is shown in Fig. 1.1. The source water is first treated to remove particulates and adjust the pH suitable for human consumption. The AOP unit then decomposes organic matter and disinfects the water. A small split stream from the treated water will be further purified via an ion exchange unit and supplied to the electrolytic cell. A power source electrolyzes water on the anode and reduces O_2 to H_2O_2 on the cathode, which supplies the AOP unit with the oxidant.

1.2 Hydrogen Peroxide

Hydrogen peroxide has an expanding market with a wide range of applications in industries including pulp and paper (50%), propylene oxide production (40%), textile, food and environmental sectors (10%). The global demand for H_2O_2 is over two million tonnes per annum. Two major commercial production methods exist: the Riedle-Pfleiderer process (over 95% of the total H_2O_2 market) and the electrochemical synthesis method [9].

1.2.1 Riedl-Pfleiderer Process

Hydrogen peroxide is predominantly manufactured by the Riedl-Pfleiderer process, which accounts for over 95% of the global production. In this process, an alkyl anthraquinone, dissolved in a mixture of polar and nonpolar solvents (such as polyalkylated benzenes and alkyl phosphates), is cycled between hydrogenation and auto-oxidation [10].

Figure 1.2 shows a simplified reaction route where the anthraquinone first undergoes hydrogenation, catalyzed by suspended Raney Ni or Pd based catalysts, to generate anthraquinol. This solution is filtered to recover the expensive catalysts, and then oxidized by air or pure oxygen to produce H_2O_2 and regenerate the anthraquinone. The product H_2O_2 is usually about 30 wt%. After liquid-liquid extraction from the organic phase to the aqueous phase and further distillation, up to 70 wt% H_2O_2 can be achieved with over 95% yield [9]. Temperature, pressure and reaction composition of the hydrogenation step are carefully controlled to mitigate excessive hydrogenation of the aromatic ring of the anthraquinone, which could lower the yield of H_2O_2. Periodic replacement of the costly quinone compound is also required to maintain the H_2O_2 yield.
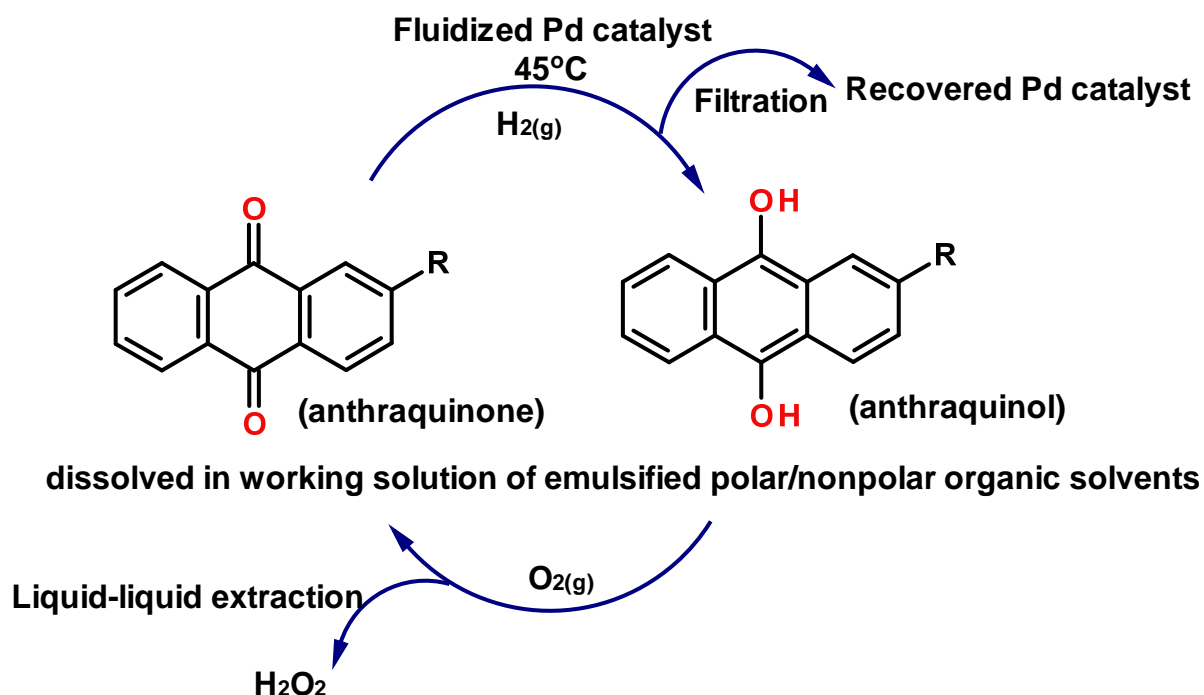
Figure 1.2 Simplified scheme of the Riedl-Pfleiderer process

The capital and energy intensive Riedl-Pfleiderer process is only advantageous with the economy of scale, and is not applicable to small scale on-site synthesis of H_2O_2.

1.2.2 Electrochemical Synthesis

Trickle-bed electrochemical cells [11] and the Dow-Huron cells [12, 13] were first developed for bleaching in the pulp and paper industry. Oloman and Watkinson [11] demonstrated a lab scale reactor with a geometric area of 0.2 m^2 that produced 3 – 4 wt% caustic peroxide at a current density of 120 mA cm^{-2} with 60% efficiency using a 2 M NaOH electrolyte. The Dow-Huron cell is an improvement to the trickle-bed reactor, which allows for better oxygen mass transfer to the cathode. A schematic single Dow-Huron cell is shown in Fig. 1.3. The cathode is composed of PTFE-bounded carbon black on porous graphite, and is operated with concurrent liquid/gas flow. The anode is typically platinized titanium or

nickel. A highly caustic (pH > 13) feed is introduced at the anode, separated from the cathode by a porous separator. The half cell reactions are:

Cathode: $O_2 + H_2O + 2e^- \rightarrow HO_2^- + OH^-$ $E^0{}_{298K} = -0.076V$ vs. SHE   (1.5)

Anode: $2OH^- \rightarrow \frac{1}{2}O_2 + H_2O + 2e^-$ $E^0{}_{298K} = -0.401V$ vs. SHE   (1.6)

Overall: $OH^- + \frac{1}{2}O_2 \rightarrow HO_2^-$ $E^0{}_{298K} = -0.477V$ vs. SHE   (1.7)
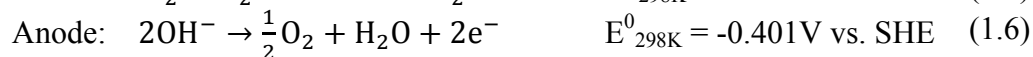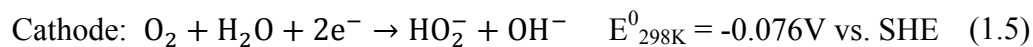
A cell operating at 2.3 V and 62 mA cm^{-2} generates 4 – 5 wt% caustic peroxide at a current efficiency of 90% [9]. Compared to the Riedl-Pfleiderer process, the Dow-Huron process is much more portable; however, it has a limited hydrogen peroxide market due to the high alkalinity of its product solution ($NaOH/H_2O_2$ weight ratio of 1.6 to 1.8). Aside from issues with peroxide decomposition under alkaline media, this high pH (14) is not suitable for drinking water treatment.
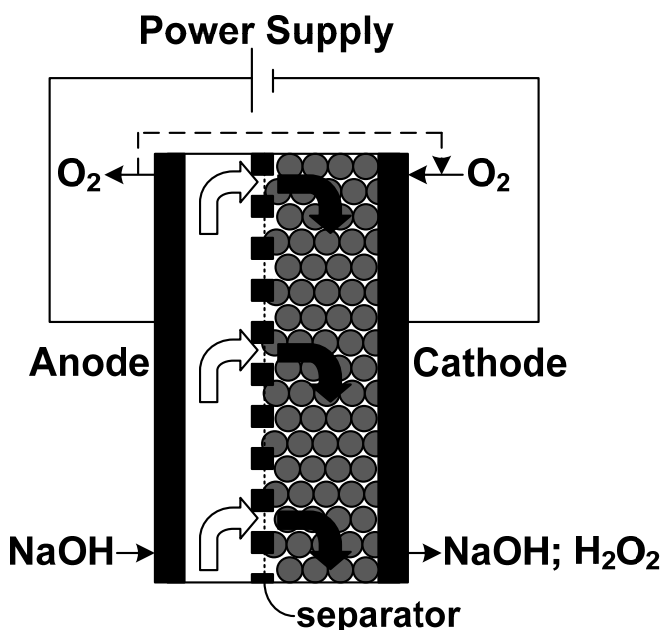
Figure 1.3. Dow-Huron electrochemical cell for H_2O_2 (adapted from Oloman[14] with permission from The Electrochemical Consultancy)

7

1.3   Objective of the Present Work

The objective of the present work is to explore quinone-based redox catalysts for the electroreduction of O_2 to H_2O_2, which could generate H_2O_2 suitable for the applications of AOP processes in drinking water treatment. Fundamental electrochemistry aspects of quinone mediated O_2 electroreduction will be studied.

The present work reports the synthesis of a novel riboflavinyl-anthraquinone compound which shows electroactive behavior immobilized on a carbon support, and redox catalytic activity for O_2 reduction to H_2O_2. Cyclic voltammetry with a rotating ring-disk electrode assembly was employed to characterize the catalyst. Chronoamperommetry experiments in a batch electrolysis cell were performed up to 24 hours to demonstrate long term H_2O_2 synthesis. This thesis project identified a quinone-based redox catalyst for the potential application in the electrosynthesis of H_2O_2 via O_2 reduction. The batch H-cell configuration presents significant O_2 mass transfer constraints. Engineering design for a three-phase catalyst layer and effective O_2 delivery setup in an electrochemical cell producing H_2O_2 in a pH neutral solution is recommended for its utilization in drinking water treatment systems.

Chapter 2: Background and Literature Review

Oxygen electroreduction plays important roles in fuel cells, corrosion and bioelectrochemistry. Two reaction pathways, depending on the electrode composition, are possible: the ultimate four-electron pathway as shown in Eqn 2.1, or the peroxide two-electron pathway as shown in Eqn 2.2. The thermo-decomposition of H_2O_2 (Eqn 2.3) can also occur, particularly under alkaline media, in the presence of transition metals, and/or at high temperatures.

$$O_2 + 4H^+ + 4e^- \rightarrow 2H_2O \qquad E^0_{298K} = 1.23 \text{ V vs. SHE} \qquad (2.1)$$

$$O_2 + 2H^+ + 2e^- \rightarrow H_2O_2 \qquad E^0_{298K} = 0.69 \text{ V vs. SHE} \qquad (2.2)$$

$$2H_2O_2 \rightarrow 2H_2O + O_2 \qquad \Delta H^0_{298K} = -100.4 \text{ kJ mol}^{-1} \qquad (2.3)$$
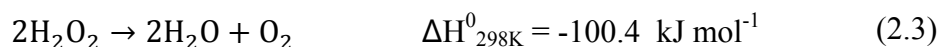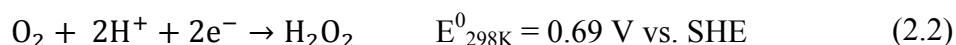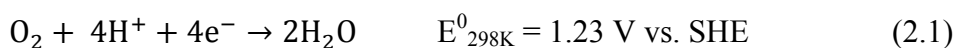
On Pt and Ag surfaces, the four-electron pathway dominates; whereas on Au and carbon surfaces the two-electron pathway prevails. From Eqns 2.1 and 2.2, it is realized that the water pathway is thermodynamically favoured; however, the high dissociation energy of O_2 (494 kJ mol^{-1}) leads to its non-labile kinetics, such that the peroxide pathway is also possible.

2.1 Carbon-based Catalysis for Oxygen Reduction

Conventional peroxide electrosynthesis processes occurs under alkaline media (pH > 13), where cabon-based electrodes show favourable O_2 reduction kinetics for caustic peroxide generation. A widely accepted mechanism was proposed by Goldstein and Tseung [15]. One *sp* orbital of the O atom overlaps with the delocalized *p* orbitals of the graphite substrate, where a dioxygen molecule adsorbs with an end-on position. As shown

by Fig 2.1, a partial electron transfer will result in hydrogen bonding with adjacent hydroxyl ions, terminated by a water molecule at a kink site. Hydrogen bonding lowers the activation energy for the subsequent electron transfer. Completion of the electron transfer followed by a reorientation of the adsorbed species produces a free HO_2^- ion.
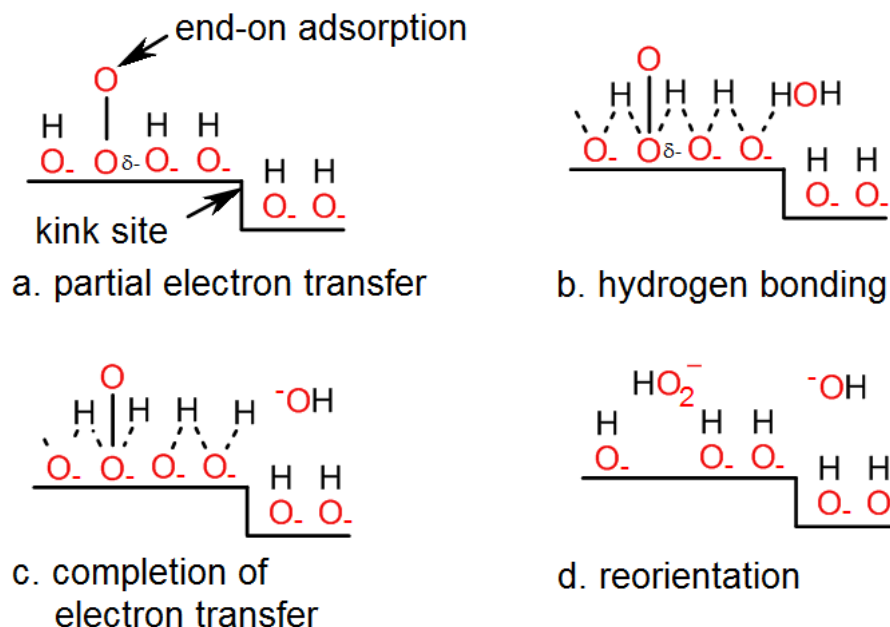
Figure 2.1 Peroxide mechanism on a carbon-based electrode (modified from Goldstein et al.[15] with permission from Nature Publishing Group)

Lateral adsorption of the dioxygen molecule results in the pseudosplitting mechanism (Fig. 2.2). Each p_x or p_y atomic orbital of the O_2 molecule forms half a bond with the delocalized p orbitals of neighbouring aromatic rings of the graphite substrate, with a stretch in the O-O bond. H bonding and the subsequent electron transfer contribute to the anti-bonding orbitals of O_2, leading to its eventual bond cleavage.

Energetically the end-on adsorption is favoured, since the lateral adsorption requires an energetic penalty of the O-O bond stretch. The peroxide mechanism is also statistically

favoured. The probability of two kink sites within proximity to the O_2 adsorption site is much less than that of just one kink site.
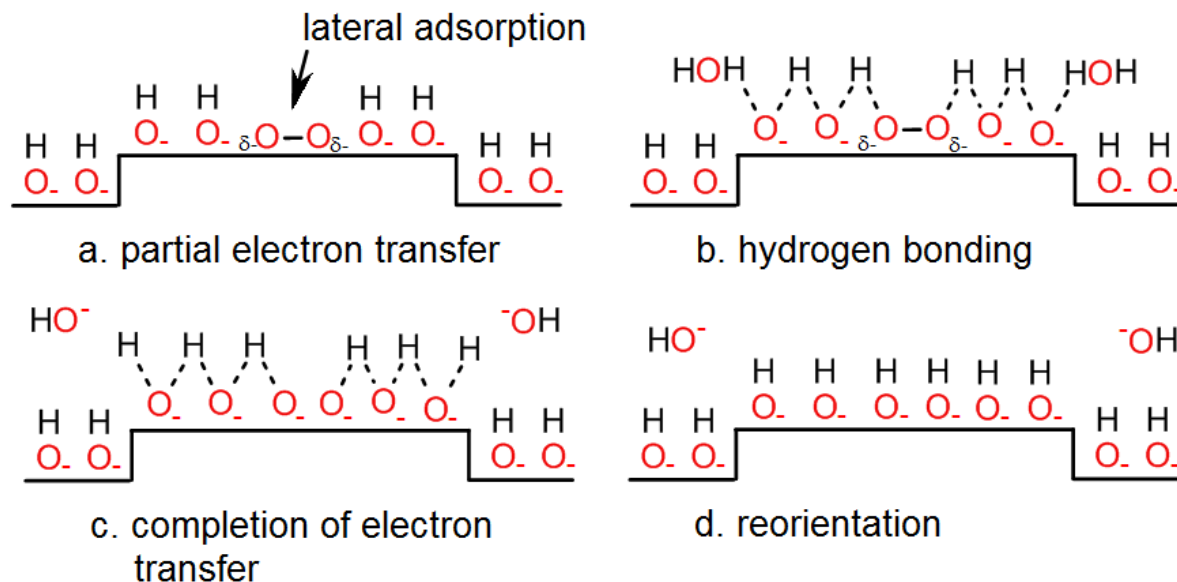
Figure 2.2 Pseudosplitting mechanism on a carbon-based electrode (modified from Goldstein et al.[15] with permission from Nature Publishing Group)

Oxygen reduction is strongly dependent on the structure of the carbon substrate. Graphite materials with few defects such as highly oriented pyrolytic graphite (HOPG) show markedly lower catalytic activity compared to glassy carbon and graphite [16].

Since the 1970's, bench scale caustic peroxide electrosynthesis cells have demonstrated success. Table 2.1 outlines the operating conditions and product peroxide concentration for selected reactors. Industrial scale application has been successful with the Dow alkaline peroxide generation plant at the Muskogee pulp mill of the Fort Howard Co., USA, generating 4 tonne day^{-1} of peroxide since 1991. The most significant drawback that prevented the widespread utilization of this process is its highly alkaline product.

Table 2.1 Caustic peroxide electrosynthesis cells with carbon-based cathodes

Reference	Davison [17]	Yamada [18]	Oloman [11]
Cell geometric area	0.025 m^2	0.8 m^2	0.0267 m^2
Cathode material	RVC foam (0.3 cm)	Carbon felt	Graphite chips (0.1 cm)
Separator type	Nafion$^®$ 426	Nafion$^®$ 117	Polypropylene diaphragm
Electrolyte	2 M NaOH	2 M NaOH	2 M NaOH
Cell voltage	2.1 V	1.3 V	1.8 V
Current density	150 mA cm^{-2}	87.6 mA cm^{-2}	120 mA cm^{-2}
Current efficiency	97.4 %	46 %	60 %
[HO$_2^-$]	0.9 M	0.45 M	0.8 M

2.2 Oxygen Reduction to Hydrogen Peroxide in Acidic Media

In acidic and neutral media, oxygen reduction on non-platinum catalysts is kinetically challenging. Transition metal N$_4$-chelates are known effective O$_2$ reduction catalysts. Wiesener et al. [19] demonstrated the activity and stability of heat treated metal porphyrin-based catalysts supported on carbon. Co-based catalysts have been the most successful in H$_2$O$_2$ synthesis. Much cheaper Co precursors such as cobalt acetate salt have also been demonstrated to match the performance of Co porphyrin [20].

Commonly, the Co precursor is heat treated with the carbon particle support to form chelate complexes. Fig. 2.3 shows a Co-tetra-porphyrin as the precursor. The N atoms with lone pair electrons behave as Lewis base and are prone to H$^+$ attack. The O$_2$ molecule adsorbs to the Co center with an end-on orientation, through the overlap of the p_x or p_y orbital

of the O atom with the d_{xz} or d_{yz} orbital of the Co atom. Such environment favours the formation of H_2O_2.
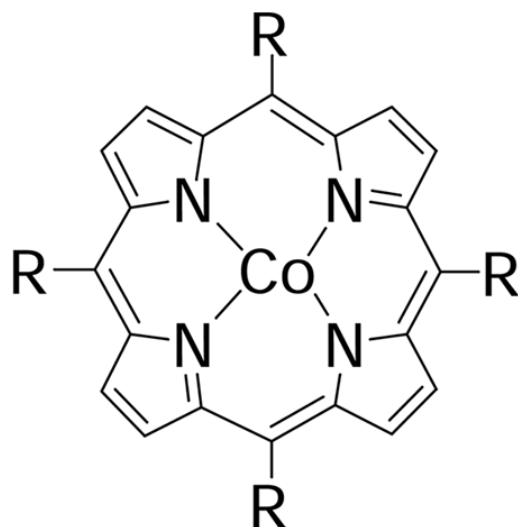
Figure 2.3 Cobalt-tetra-porphyrin structure

From the catalyst heat treatment process, the face-to-face porphyrins (Fig 2.4) may also form. Yeager [21] showed that when the Co-Co distance is about 4 Å, as to permit the formation of an –O-O– bridge, the O-O bond weakens. Such environment favours the formation of H_2O.
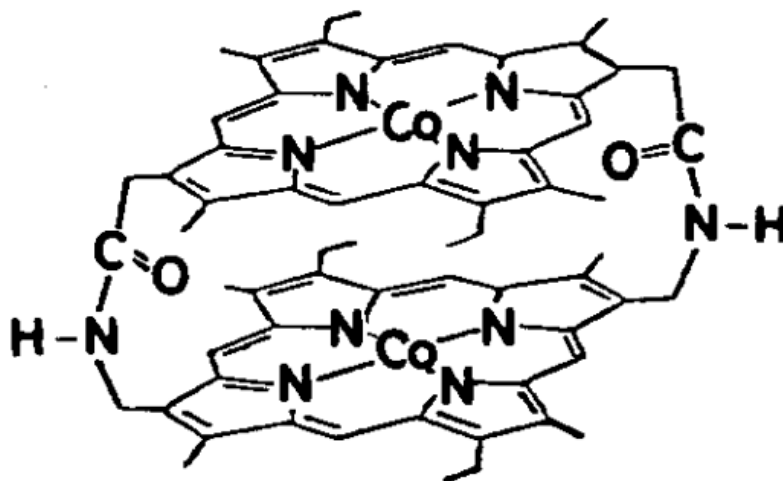
Figure 2.4 Face-to-face Co-Co 4-porphyrins (adapted from Yeager [21] with permission from Elsevier)

13

Bonakdarpour et al. [22] prepared catalysts using the simple $Co(NO_3)_2$ precursor, and demonstrated 5 µmol cm^{-2} h^{-1} H_2O_2 production in a flooded batch electrosynthesis cell using dissolved O_2 in 0.5 M H_2SO_4 with current efficiencies of 85 ± 5% at 0.25 V vs. RHE.

2.3 Oxygen Reduction on Quinone-modified Electrodes

A different mechanism for oxygen reduction via graphite catalysis, proposed by Xu et al. [23] considers the electrocatalytic (redox) mediation by surface quinones. This mechanism suggests that quinone radical anions form in the one electron reduction of native quinone-type functionalities on carbon surfaces. The semi-quinone radical then mediates the reduction of O_2 to $O_2^{\bullet-}$ in a rate determining step (Eqn 2.5). The subsequent disproportionation of the superoxide radical with H_2O, thus forms H_2O_2. The elementary reaction steps of this mechanism are presented as follows,

$$Q + e^- \rightarrow Q^{\bullet-} \tag{2.4}$$
$$Q^{\bullet-} + O_2 \rightarrow Q + O_2^{\bullet-} \tag{2.5}$$
$$2O_2^{\bullet-} + H_2O \rightarrow O_2 + HO_2^- + OH^- \tag{2.6}$$
$$\text{or}$$
$$O_2^{\bullet-} + H_2O + e^- \rightarrow HO_2^- + OH^- \tag{2.7}$$
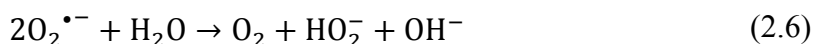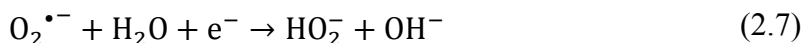
This mechanism also suggests that the further reduction of the semi-quinone radical to the dianion (Eqn 2.8), is not active towards O_2 reduction.

$$Q^{\bullet-} + e^- \rightarrow Q^{2-} \tag{2.8}$$

Gyenge and Oloman used an emulsion of 2-ethylanthraquinone with a cationic surfactant, and reticulated vitreous carbon and graphite felt as the cathode to produce up to 0.6 M of H_2O_2 in 2 M Na_2SO_4 electrolyte at 80 mA cm^{-2} with about 50% current efficiency [24, 25]. Much research has focused on electrode modifications with quinones and similar

functional compounds [26-38]. Methods of surface immobilization included: irreversible adsorption [26, 32], covalent attachment of diazonium salts of quinones [29-31], and anodic polymerization of amino-anthraquinone over the electrode surface [27, 28, 33]. Adsorptive attachment entails the easiest preparation procedure; however, long term operation in alkaline solutions may lead to desorption from the surface. Covalent attachment provides a stronger attachment. Berchmans and Vijayavalli [34] attached riboflavin to glassy carbon electrodes through covalent linkage of the amine or alcohol groups to the surface carboxylic groups of the carbon substrate. Manisankar et al. [35, 36] modified the electrode described by Berchmans and Vijavavalli with several 9,10-anthraquinones and reported that riboflavin was beneficial to the quinone reduction and thus, the subsequent rate of O_2 reduction in buffered pH neutral electrolytes increased as well. The majority of these investigations involved modification of glassy carbon electrodes, where the presence of quinones or riboflavin (on the order of 10^{-9} mol cm^{-2}) shifts the potential of O_2 reduction to more positive values.

From the literature, it has been identified that riboflavin, 9,10-anthraquinones, and phenanthrenequinone show the most promise. For practical electrocatalysis, high surface area carbon support such as Vulcan XC72 is typically employed. Lobyntseva et al. [30] prepared a membrane-electrode assembly with Vulcan XC72 grafted with diazonium-anthraquinone as the cathode, but the H_2O_2 current efficiencies were less than 1 %. Lobyntseva et al. attributed the low H_2O_2 yield to sub-optimized reactor design; however no further update has been reported since.

This thesis project attempts to study the catalytic activity of the identified promising compounds supported on Vulcan XC72.

2.4 Brief Background of Electroactive Films and Modified Electrodes [39]

Surface modified electrodes are commonly prepared by modifying a conductive substrate to produce an electrode suited to a particular function. Several techniques for the modification can be achieved by: irreversible adsorption, covalent attachment of a monolayer, or coating with a polymer film. Irreversible adsorption occurs generally when the substrate environment is more energetically favourable for the adsorbate than the aqueous or gaseous phase; the adsorption thereafter lowers the surface energy of the system. Many organic compounds, especially aromatic rings, double bonds and long hydrocarbon chains, irreversibly adsorb onto metal or carbon surfaces. For stronger attachment, covalent linkage of the desired component to the surface groups present, or formed, on the substrate can be accomplished. Modifications by polymer films can result in electroactive layers thicker than a monolayer. One common technique is via electrodeposition, where oxidation (or reduction) of the monomer forms a polymer coating on the substrate.

The electrochemistry of adsorbed films is different from the purely diffusional case. For a system involving both an adsorbed film and its dissolved phase, the treatment will be more complicated and requires an appropriate adsorption isotherm model.

2.4.1 Adsorption Isotherms

The relationship between the adsorbed state and the solution state of a species, i, in equilibrium can be characterized by an adsorption isotherm. At equilibrium, the potentials of species i in the adsorbed state and the bulk solution state are equal as follows:

$$\bar{\mu}_i^{0,A} + RT \ln a_i^A = \bar{\mu}_i^{0,b} + RT \ln a_i^b \qquad (2.9)$$

where the superscripts A and b refer to the adsorbed and the bulk states, respectively, $\bar{\mu}_i^0$ terms are the standard electrochemical potentials, and a_i is the activity of species i.

Incorporating the standard free energy of adsorption, $\Delta\bar{G}_i^0$, activities of the two states can be related as follows:

$$a_i^A = a_i^b \exp\left(-\frac{\Delta\bar{G}_i^0}{RT}\right) = \beta_i a_i^b \qquad (2.10)$$

Several adsorption isotherms have seen wide applications. The Langmuir and Frumkin isotherms are amongst the most popular:

$$\frac{\Gamma_i}{\Gamma_{mon} - \Gamma_i} = \beta_i a_i^b \qquad (2.11)$$

$$\frac{\Gamma_i}{\Gamma_{mon} - \Gamma_i} \exp\left(-\frac{2g\Gamma_i}{RT}\right) = \beta_i a_i^b \qquad (2.12)$$

where Γ_i and Γ_{mon} represent the surface coverage and saturated monolayer coverage, respectively, and g is a correction parameter to the free energy of adsorption.

The Langmuir isotherm assumes no intermolecular interaction between the adsorbed and bulk states, and no heterogeneity on the surface (and thus a constant free energy of adsorption); whereas the Frumkin isotherm assumes a linear dependence of the free energy of adsorption on the surface coverage. Since β_i considers the electrochemical Gibb's free energy, the monolayer adsorption is also a function of the electrode potential.

2.4.2 Electrochemistry of Adsorbed Films

First, let us consider the more general case of a system involving both an adsorbed film and its diffuse phase. The governing flux equation at the electrode surface can be expressed as follows:

$$D_{Ox}\left[\frac{\partial C_{Ox}(x,t)}{\partial x}\right]_{x=0} - \frac{\partial \Gamma_{Ox}(t)}{\partial t} = -\left[D_{Re}\left(\frac{\partial C_{Re}(x,t)}{\partial x}\right)_{x=0} - \frac{\partial \Gamma_{Re}(t)}{\partial t}\right] \tag{2.13}$$

$$= \frac{i}{1000nF}$$

where Ox and Re are the oxidized and reduced species, respectively; D_j and C_j are the diffusion coefficient and bulk concentration of species j, respectively. i is the net current density through the electrode.

To solve this equation, along with the initial conditions of the surface coverage, Γ and C must be related by an appropriate adsorption isotherm. Applying the linearized Langmuir isotherm, those relationships are as follows:

$$\Gamma_{Ox}(t) = \frac{\beta_{Ox}\Gamma_{Ox,mon}a_{Ox}(0,t)}{1 + \beta_{Ox}a_{Ox}(0,t) + \beta_{Re}a_{Re}(0,t)} \tag{2.14}$$

$$\Gamma_{Re}(t) = \frac{\beta_{Re}\Gamma_{Re,mon}C_{Re}(0,t)}{1 + \beta_{Ox}a_{Ox}(0,t) + \beta_{Re}a_{Re}(0,t)} \tag{2.15}$$

2.4.3 Voltammetry of Irreversibly Adsorbed Thin Films – Nernstian Behavior

For the case where the electroactive film is irreversibly adsorbed and there is no dissolved phase, Eqn 2.13 becomes as shown:

$$-\frac{\partial \Gamma_{Ox}(t)}{\partial t} = \frac{\partial \Gamma_{Re}(t)}{\partial t} = \frac{i}{1000nF} \tag{2.16}$$

It is also realized that

$$\Gamma_{Ox} + \Gamma_{Re} = \Gamma^* = \text{constant} \tag{2.17}$$

From the definition of a Nernstian behavior,

$$\frac{C_{Ox}(0,t)}{C_{Re}(0,t)} = \exp\left[\frac{nF}{RT}(E - E^0)\right] \tag{2.18}$$

Eliminating C_{Ox} and C_{Re} from Eqns. 2.14 and 2.15,

$$\frac{\Gamma_{Ox}(t)}{\Gamma_{Re}(t)} = \left(\frac{\beta_{Ox}\Gamma_{Ox,mon}}{\beta_{Re}\Gamma_{Re,mon}}\right)\exp\left[\frac{nF}{RT}(E - E^0)\right] \tag{2.19}$$

From Eqn 2.16, followed with the assumption that the Ox and Re adsorption isotherms are identical ($\beta_{Ox}\Gamma_{Ox,mon} = \beta_{Re}\Gamma_{Re,mon}$),

$$i = \frac{1000n^2F^2}{RT}\frac{\upsilon\Gamma^* \exp[(nF/RT)(E - E^0)]}{\{1 + \exp[(nF/RT)(E - E^0)]\}^2} \tag{2.20}$$

where υ is the potential sweep rate ($\partial E/\partial t$).

A typical Nernstian cyclic voltammogram is presented in Fig. 2.5, where the peak current and the width at half-height can be expressed as follows,

$$i_p = \frac{1000n^2F^2}{4RT}\upsilon\Gamma^* \tag{2.21}$$

$$\Delta E_{p,1/2} = 3.53\frac{RT}{nF} \tag{2.22}$$
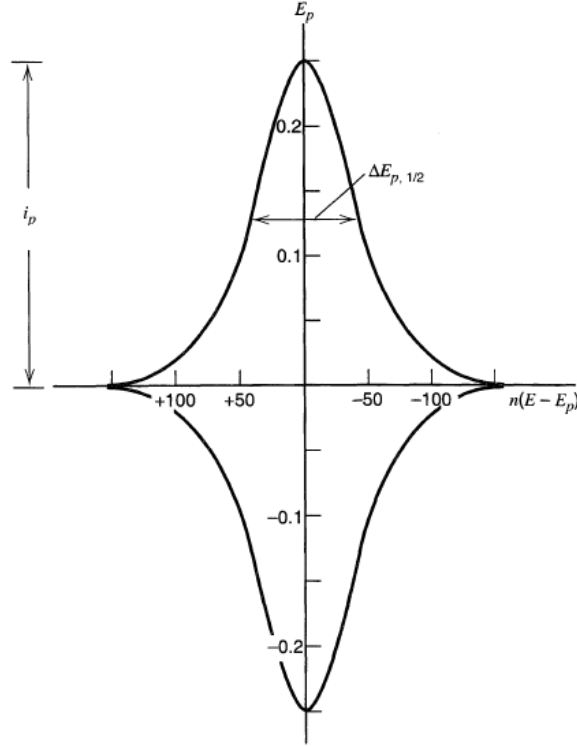
Figure 2.5 Typical Nernstian cyclic voltammogram (adapted from Bard et al.[39] with permission from Wiley)

2.4.4   Voltammetry of Irreversibly Adsorbed Thin Films – Irreversible Behavior

With the same irreversibly adsorbed electroactive film, if the electrochemical reaction is irreversibly with respect to the potential sweep rate, the Nernstian boundary condition in 2.3.3 is replaced with a kinetic boundary condition as follows:

$$\frac{i}{1000nF} = k_f \Gamma_{Ox}(t) \tag{2.23}$$

$$k_f = k^0 \exp[-(\alpha F/RT)(E - E^0) + \alpha \upsilon (F/RT)t] \tag{2.24}$$

where k^0 is the standard rate constant, and α is the transfer coefficient.

From Eqn 2.23 and the initial condition of the surface coverage Γ^*,

$$\frac{d\Gamma_{Ox}}{dt} = -k_f \Gamma_{Ox} \tag{2.25}$$

20

$$\Gamma_{Ox} = \Gamma^* \exp\left(\frac{RT}{\alpha F}\frac{k_f}{\upsilon}\right) \tag{2.26}$$

Substituting Eqn 2.26 to 2.23, the current response from voltammetry can be expressed as follows:

$$i = 1000 F k_f \Gamma^* \exp\left(\frac{RT}{\alpha F}\frac{k_f}{\upsilon}\right) \tag{2.27}$$

A typical irreversible linear voltammogram is presented in Fig 2.6, where the peak current and the width at half-height can be expressed as follows,

$$i_p = \frac{1000\alpha F^2 \upsilon \Gamma^*}{2.718 RT} \tag{2.28}$$

$$\Delta E_{p,1/2} = 2.44\frac{RT}{\alpha F} \tag{2.29}$$
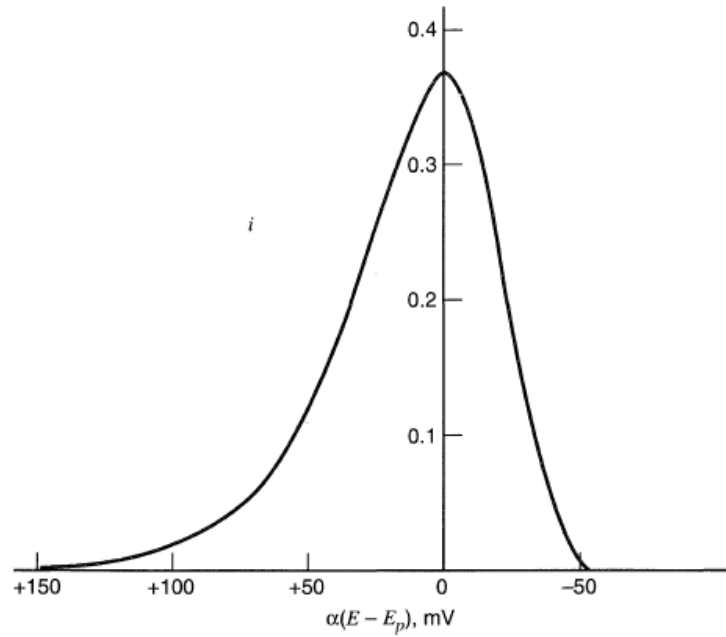
Figure 2.6 Typical irreversible linear voltammogram (adapted from Bard et al.[39] with permission from Wiley)

Chapter 3: Experimental Method

The experimental work entailed in this thesis project include the synthesis of the redox catalyst, its characterization via Fourier transform IR spectroscopy, the electrocatalytic behavior investigated by static and rotating electrode cyclic voltammetry, and finally a 24 hour batch electrosynthesis in a two-phase (electrodes submerged in aqueous solutions) electrochemical cell to demonstrate the catalyst's performance.

3.1   Chemicals

The quinone compounds and riboflavin were purchased from Sigma-Aldrich at the highest purity available and used directly without further purification. All solutions were prepared with deionized water of 18.2 $M\Omega$ cm^{-1} resistivity at $21^{o}C$ (Siemens Purelab). Cyclic voltammetric measurements were performed in 0.1 M H_2SO_4, and batch electrolysis was conducted in 0.5 M H_2SO_4.

A list of chemicals and materials with their sources and grade is shown in Table 3.1. The Nafion membrane was treated by a three-step boiling process to remove organic and metallic contaminants. The membrane was boiled in 3 wt/v% H_2O_2 at approximately 90 ^{o}C for 30 minutes, followed by boiling in DI water and then in 0.5 M H_2SO_4 sequentially in the same fashion. The treated membrane was kept submerged in DI water.

Table 3.1 Chemicals and materials

Chemical	Grade	Source
Carbon powder	Vulcan XC72	Cabot Inc.
Carbon paper	Toray® TGP-H-60, 190 microns thick (no Teflon treatment)	Fuel Cell Earth
Nafion® solution	5 wt/v%	Alfa Aesar
Nafion® membrane	112 (0.002" thick)	Dupont
Quinone Compounds		
Anthraquinone-2-carboxylic acid (CAQ)	98 wt%	Sigma-Aldrich
1,2-diamino-anthraquinone (DAAQ)	98 wt%	Sigma-Aldrich
2-ethyl-anthraquinone (EAQ)	97 wt%	Sigma-Aldrich
Phenanthrenequinone (PQ)	99 wt%	Sigma-Aldrich
Riboflavin (RF)	98 wt%	Sigma-Aldrich
Solvents and Reagents		
Thionyl chloride ($SOCl_2$)	> 99 v%	Fluka
Pyridine (py)	Certified ACS	Fisher Scientific
Hexanes	Certified ACS	Fisher Scientific
Ethanol	Certified ACS	Fisher Scientific
Salts and others		
Sulfuric acid (H_2SO_4)	Certified 95 – 98 wt/v%	GFS Chemicals
Potassium sulfate (K_2SO_4)	Certified ACS	Fisher Scientific
Potassium iodide (KI)	Certified ACS	Fisher Scientific
Potassium hydrogen phthalate (KHP)	Certified ACS	Fisher Scientific
Ammonium molybdate tetrahydrate	ACS	Fisher Scientific
Hydrogen Peroxide (H_2O_2)	3 wt/v% Certified	Fisher Scientific
Nitrogen (N_2)	99.998 v%	Pexair
Oxygen (O_2)	99.993 v%	Pexair
Hydrogen (H_2)	99.999 v%	Pexair
Alumina micropolish	0.05 micron	Guehler

3.2 Synthesis of riboflavinyl-anthraquinone-2-carboxylate ester

Riboflavinyl-anthraquinone-2-carboxylate ester (RF-AQ) was synthesized as shown in Eqn 3.1, and graphically in Fig. 3.1. Four grams of CAQ was first chlorinated with 50 mL of thionyl chloride refluxed at $80\,^{\circ}C$ for three hours in a round-bottom flask immersed in an oil bath. Total reflux was achieved by a spiral condenser with cooling water, as demonstrated by Fig 3.1a.

(3.1)
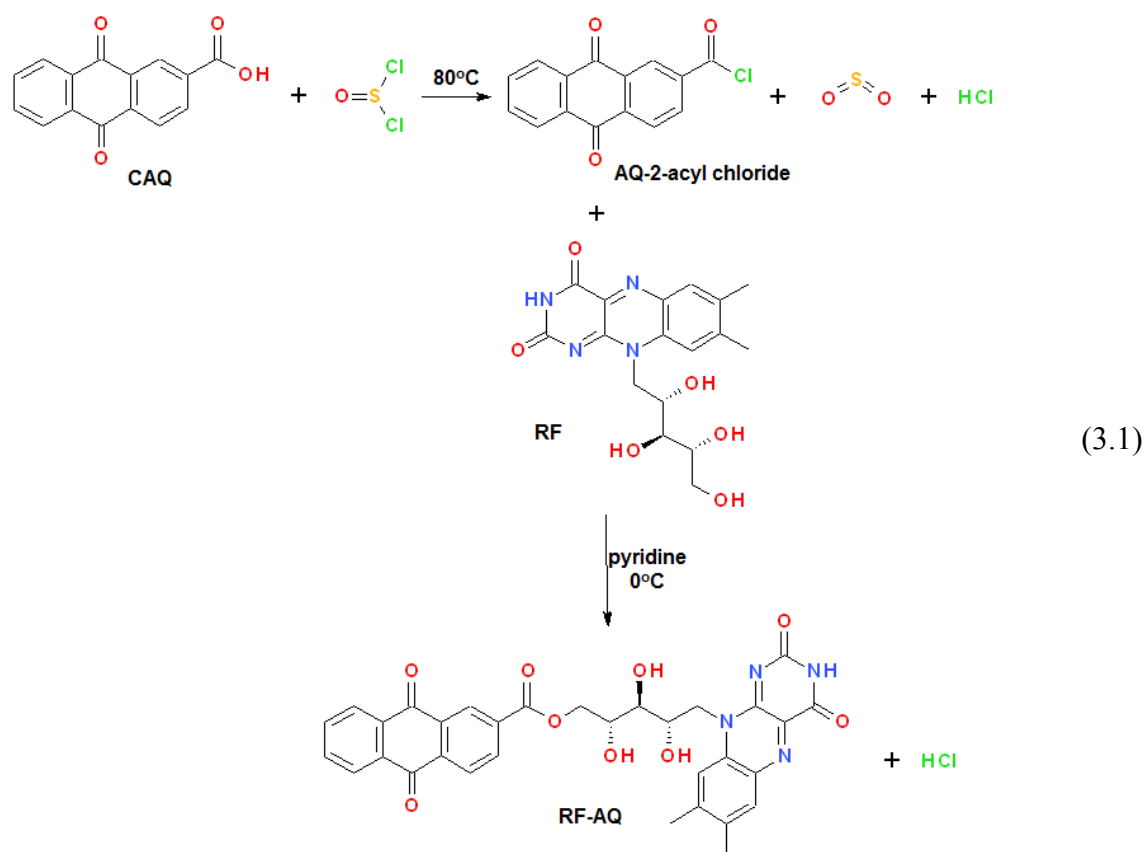
The solution first appeared murky brown then turned clear brown as the reaction proceeded. After the three hour reflux, the excess thionyl chloride was distilled off (Fig. 3.1b). The remaining product was a consistent yellow-green solid. The product acyl chloride was then dissolved in 50 mL of pyridine at 0 $^{\circ}$C in an ice bath (Fig. 3.1c). It is important that the pyridine used has low water content. Water will react violently with the acyl chloride, producing a cloud of steam and HCl.

Riboflavin (stochiometric ratio of 1.1 to AQ) was then slowly added to the acyl chloride solution with constant stirring. After the reaction had subsided, the excess pyridine was distilled off at 100 $^{\circ}$C (Fig. 3.1d). A side reaction between pyridine and HCl produces pyridinium chloride. Because of its high solubility in water, it was effectively eliminated by washing and vacuum filtration (Fig. 3.1e).
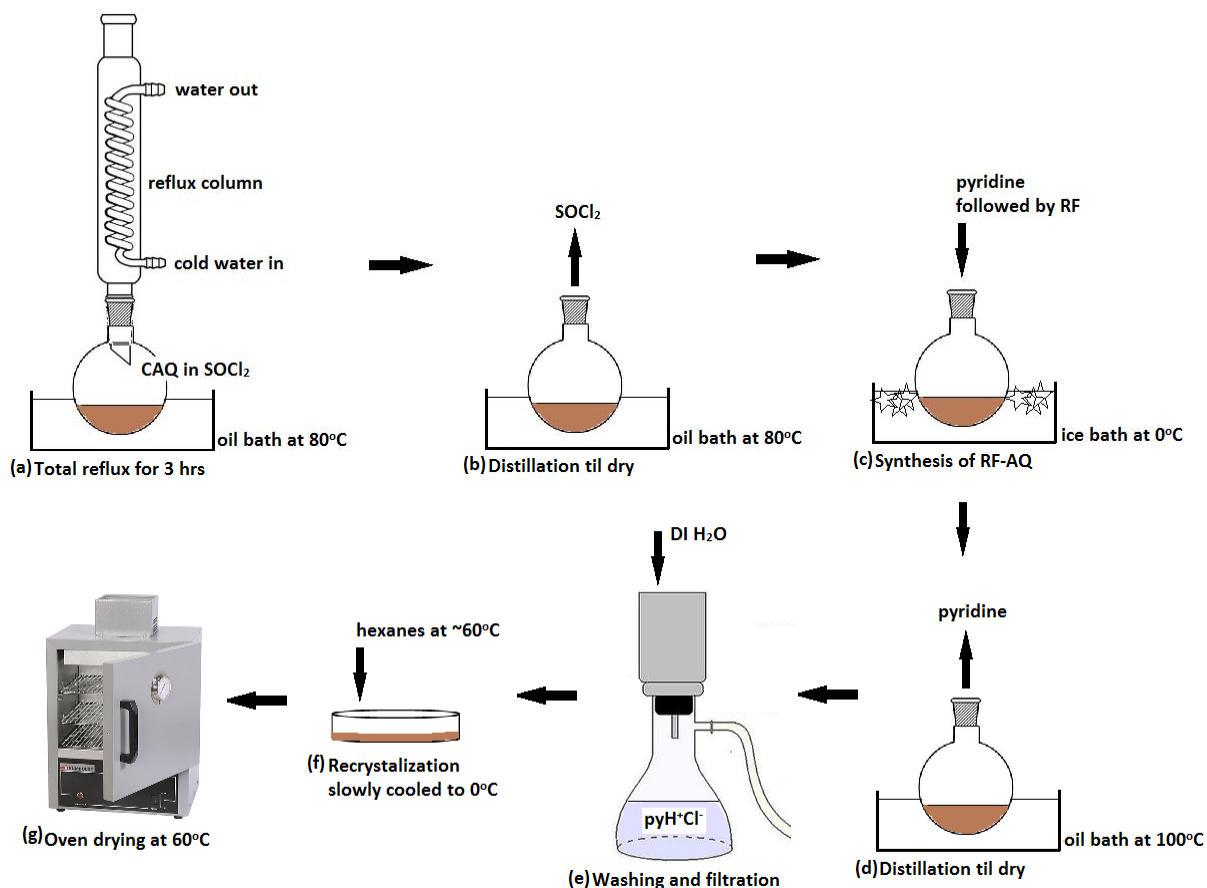
Figure 3.1 Total reflux column for RF-AQ synthesis

The final product was then purified by recrystalization in hexanes (Fig. 3.1f). The hexanes solution was brought to just before a gentle boil at approximately 60 $^{\circ}$C. The hot hexanes solution was slowly added to the solid product until all the solid had dissolved at this temperature. It was then slowly allowed to cool to room temperature, and chilled briefly in an ice bath before vacuum filtration. The slow cooling allowed for consistent and preferential crystallization of the desired product. The pure RF-AQ product was dried in the oven at 80 $^{\circ}$C overnight (Fig. 3.1g). The final product is a yellow powder. Because of the many purification processes that have not been optimized, the yield, per CAQ, was only about 20 %.

3.3   Fourier Transform Infrared Spectroscopy

Fourier transform infrared spectroscopy was used to characterize the RF-AQ compound.   This technique utilizes the phenomenon that molecules absorb radiation at specific frequencies characteristic of their structure. These resonant frequencies are a direct consequence of the molecular potential energy surfaces and the atomic masses of the constituents, corresponding to the quantized vibrational and rotational energy level changes.

Rotational energy level transitions contribute to discrete lines on the IR spectrum, whereas transitions in the vibrational energy levels appear as bands.   To identify organic compounds, the vibrational-rotational bands occurring in the region of $4000 - 400$ cm^{-1} are typically employed.   The two fundamental modes are stretching and bending.

IR radiation is absorbed when the oscillating dipole moment, due to a molecular vibration, interacts with the oscillating electric field of the incidental IR beam.   Therefore, the larger the change in the dipole moment, the more intense the absorption peak is.

The Brunker IFS 55 Fourier transform infrared (FTIR) spectrometer was used for the spectra collection in the mid IR range (4000 to 400 cm^{-1}) with a resolution of 0.5 cm^{-1}. About 1 mg of the sample powder was mixed with about 100 mg of dry KBr powder.   The mixture was then pressed with dies to give a transparent disc.   KBr is practically infrared transparent and thus does not interfere with the IR spectra.   The compressed disc was placed in the sample holder inside the N_2 filled chamber of the Brunker IFS 55 system, where water was effectively eliminated.   Non-monochromatic IR beams were used, and the spectral information was processed by Fourier transformation to produce the final IR spectra.

3.4   Molecular Volume Estimation for RF-AQ

To estimate the monolayer coverage of RF-AQ on the carbon support, the Hartree-Fock computational chemistry method was employed to estimate its ground state molecular volume. A trial version of CambridgeSoft ChemBio 3D software was used to perform the computation using the Hartree-Fock method with the Gaussian algorithm and 6-31G basis set [40, 41].

Since only the Schrödinger equation for H-like systems can be fully expressed, computational chemistry methods for multi-body systems are mathematical constructs which approximate the real molecular orbitals. This section presents a brief and qualitative introduction to the Hartree-Fock theory.

The Hartree-Fock method solves the time-independent Schrödinger equation invoking the Born-Oppenheimer approximation, which separates the molecular wavefunction into its electronic and nuclear components. The major assumption of this theory is that each electron can be described by a single-particle function, and does not explicitly depend on the motions of other electrons. The wavefunction of the many-body system is then given by a single Slater determinant to satisfy the antisymmetry principle and Pauli's exclusion principle. The ground state of the molecule is obtained after iterative calculations until self-consistency is achieved.

The molecular volume was then determined by an isosurface containing 99% of the electron density. The specific surface area of Vulcan XC72 is reported to be about 200 m^2 g^{-1} [42]. The monolayer loading of RF-AQ was estimated from its molecular volume and the specific area of the Vulcan XC72 support.

3.5   Catalyst Ink and Electrode Preparation

The catalyst in this thesis refers to the composite of the organic redox catalyst and the Vulcan XC72 carbon powder. The appropriate amount of quinone or riboflavin redox catalyst and Vulcan XC72 powder was sonicated in 280 µL of DI water and 70 µL of ethanol for 15 minutes, followed by the addition of 100 µL of 5 wt% Nafion solution (Alfa Aesar) and sonication for 30 minutes to make a well-mixed suspension.

For cyclic voltammetric (CV) measurements, 7 µL of the ink was placed on the glassy carbon (GC) disk electrode and air dried at $21^{\circ}C$ to achieve a catalyst loading of 0.66 mg $cm^{-2}_{geo.}$ (10 wt%). The typical weight ratio of the dry catalyst is 1:9:4.4 in the order of redox catalyst:Vulcan XC72:Nafion. The percentage catalyst loadings reported in this thesis paper refer to the weight amount of the redox catalyst per weight amount of the composite catalyst (redox catalyst and Vulcan XC72), excluding the Nafion® content. The Nafion® loading is explicitly expressed.

For electrolysis measurements, Toray® paper with no Teflon® treatment (TGP-H-060 Fuel Cell Earth) was cut into 2 cm × 2 cm squares with a 0.5 cm stem for electrical connection. The catalyst ink was deposited on the 4 cm^2 electrode in aliquots of 25 µL, followed by air drying at $21^{\circ}C$. After the entire area of the electrode was covered with the desired amount of the catalyst, it was dried in an oven at 80 $^{\circ}C$ for 12 hours. Total dry catalyst (the organic redox catalyst, Vulcan XC72 and Nafion) loadings of 1.7 to 3.5 mg $cm^{-2}_{geo.}$ were determined by weighing the electrode before and after the deposition.

3.6   Electrochemical Methods

Electrochemical measurements were performed to screen the electroactive catalysts and to characterize the catalytic activity and kinetics of the two electron reduction of O_2 to H_2O_2. For such characterizations, cyclic voltammetry (CV) using static and rotating electrodes was employed. For long term H_2O_2 generation and catalyst durability demonstration, the two-chamber (H-cell) batch electrolysis experiment was used with Toray® paper coated with the redox catalyst.

3.6.1   Cyclic Voltammetry

Cyclic voltammetric (CV) measurements were performed using the CBP Bipotentiostat system (Pine Instruments). The working electrode assembly consisted of a Pine (AFE6R2GCPT) rotating ring disk electrode (RRDE), shown in Fig 3.2, with a glassy carbon disk (0.2376 $cm^2_{geo.}$) and a platinum ring (0.2356 $cm^2_{geo.}$) with a collection efficiency of about 38 %. The disk and ring electrodes are separated by a Teflon® spacer.

Figure 3.2 Rotating ring disk electrode assembly

The electrode surface was polished with 0.05 µm alumina micropolish to a mirror finish before each experiment. 7 µL of the catalyst ink was dropped onto the glassy carbon

disk, and allowed to air dry at room temperature. The RRDE assembly was then attached to the rotator and its tip was immersed in about 100 mL of the 0.1 M H_2SO_4 electrolyte.

A typical four-electrode configuration, shown in Fig. 3.3, was setup in a single-compartment electrochemical cell. A Pt wire electrode (Radiometer Analytical) was used as the counter electrode; while a $Hg/HgSO_4$ electrode was used as the reference electrode. O_2 was purged in the electrolyte through a 5 μm porous dispersion tube (Ace Glass) for 30 minutes before each experiment, and a gas atmosphere was maintained above the electrolyte for the duration of each experiment to maintain O_2 saturation in the electrolyte. N_2 was purged in the electrolyte for de-aerated experiments.
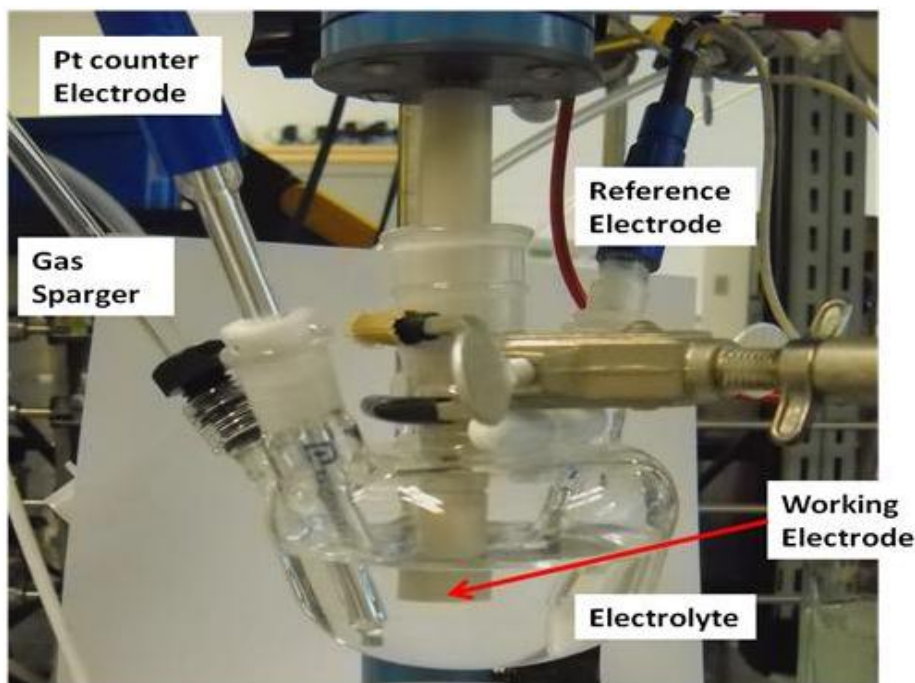

Figure 3.3 Four electrode configuration for RRDE

All experiments were performed at 21 ± 0.5 ^oC and 1 bar_{abs}. The Pt ring electrode was cleaned by cycling between $0 - 1.2$ V vs. RHE until steady state CVs were obtained.

During the measurements, the ring electrode was held constant at 1.2 V vs. RHE to record the H_2O_2 oxidation current.

First, a CV in the N_2-purged electrolyte was recorded to characterize the redox behavior of the quinone-based catalysts. Next, O_2 was purged for 30 minutes in the electrolyte, and its saturation in the electrolyte was maintained by allowing for an O_2 blanket over the solution for the short-term duration of the O_2 reduction reaction (ORR). ORR was performed with the RRDE assembly rotating at fixed rotation speeds of 100, 400 and 900 RPM. After the ORR, a second CV measurement in the N_2-purged electrolyte was againéd performed to determine the adhesion of the quinone-based catalysts on the carbon support.

3.6.2   Chronoamperommetry

Bulk electrolysis experiments were performed using an H-cell (Fig. 3.4) connected to the same CBP Bipotentiostat system. The anode and cathode were housed in chambers separated by a Nafion® 112 membrane (12.57 cm^2). The cathode was prepared by coating a 2 cm x 2 cm piece of Toray® paper 190 µm in thickness, with the redox catalyst as described in Section 3.5. A Pt wire was used as the anode, and the 4 cm^2 area of the working electrode deposited with the redox catalyst was immersed in the electrolyte in the cathode chamber. A Hg/Hg_2SO_4 reference electrode was placed in the reference electrode chamber connected to the cathode chamber by a porous ceramic frit. The cathode was fixed at 0.1 V vs. RHE throughout the 24 hour duration of the electrosynthesis experiments.

An aliquot of 0.5 M H_2SO_4 solution was used as the electrolyte to provide sufficient ionic conductivity and protons for the reaction. Moreover, the flooded batch electrolysis cell setup provides a qualitative indication of the catalyst's performance in solid polymer fuel

cells employing a Nafion® membrane. O_2 was purged in the catholyte for 30 minutes before the experiments and continued during the experiments to maintain O_2 saturation. The cathodic chamber contained 136 mL of the electrolyte with constant stirring. Samples of 3.5 mL were periodically taken from the cathode chamber and replaced with fresh electrolyte.

All experiments were performed at 1 bar$_{abs}$, and either 21 ± 0.5 or 50 ± 0.5 ^{o}C. An isothermal water bath was employed for experiments at 50 ± 0.5 ^{o}C. Warm water was circulated in the water jacket around the cathode chamber for 30 minutes before and continued for the entire duration of the experiments.
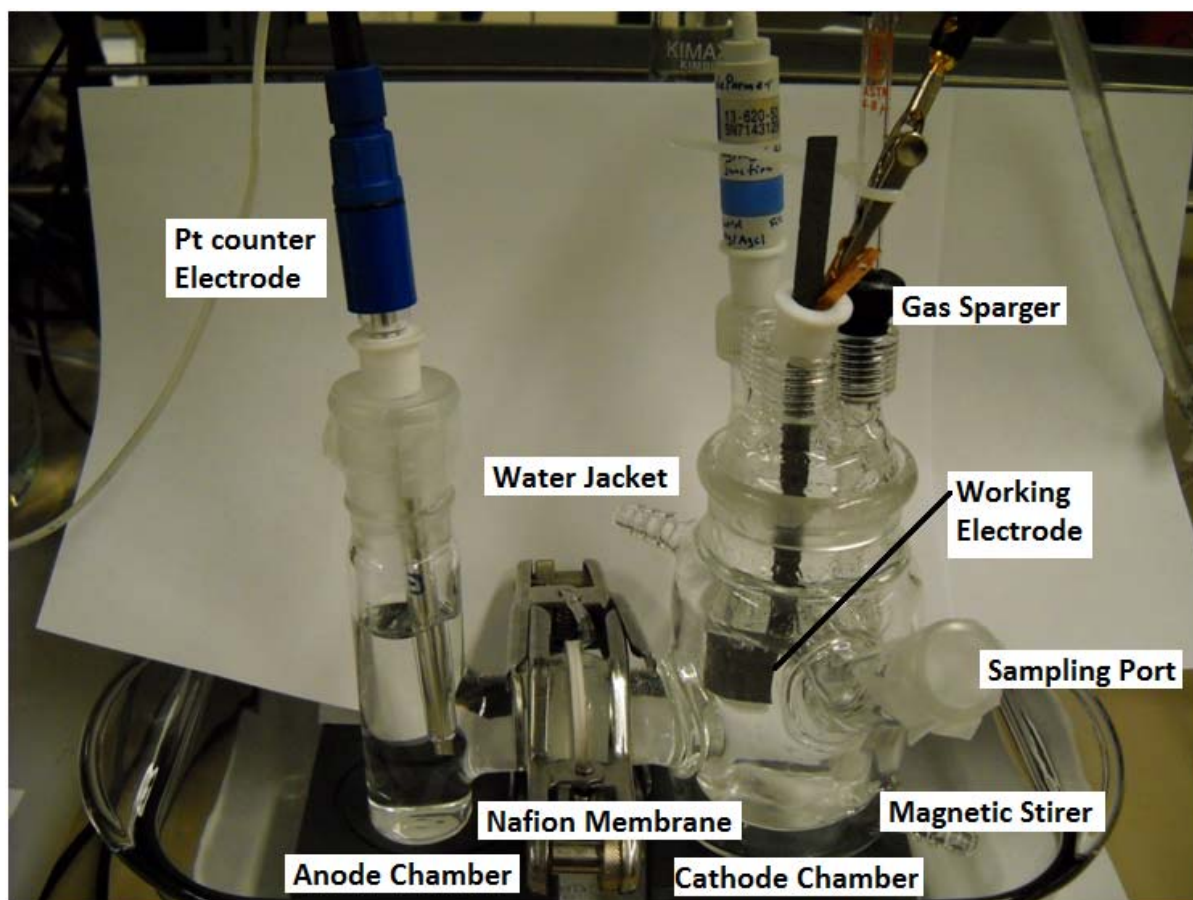
Figure 3.4 H-cell setup for batch electrolysis

3.6.3 Reference Electrode Calibration

All potential measurements reported are referenced to the reversible hydrogen electrode (RHE) scale. The RHE scale for the Hg/Hg_2SO_4 reference electrode was established by purging H_2 in the electrolyte and in contact with a Pt wire working electrode. The Hg/Hg_2SO_4 reference electrode was used as the counter electrode. The open circuit potential difference between the two electrodes provides the conversion factor between the Hg/Hg_2SO_4 scale to the RHE scale. Table 3.2 outlines the determined potential differences between the RHE and the Hg/Hg_2SO_4 electrode in different electrolytes.

Table 3.2 RHE vs. Hg/Hg_2SO_4 in various electrolytes

Electrolyte	RHE vs. Hg/Hg_2SO_4
0.1 M H_2SO_4	- 710 mV
0.5 M H_2SO_4	- 700 mV
0.1 M K_2SO_4	- 990 mV
0.1 M NaOH	- 1335 mV

3.7 UV-Vis for H_2O_2 Concentration Determination

The concentration of H_2O_2 was deteremined by the UV-Vis spectrophotometric method described by Klassen et al. [43]. This method employs the oxidation of I^- by H_2O_2, and the subsequent equilibrium between I^- and I_3^-, as follows,

$$H_2O_2 + 2I^- \rightarrow 2OH^- + I_2 \qquad\qquad (3.2)$$

$$I_2 + I^- \leftrightarrow I_3^- \qquad\qquad (3.3)$$

For the analysis, 0.5 mL of the unknown H_2O_2 sample is added to make a 10 mL solution of potassium hydrogen phthalate (KHP 24.5 mM), NaOH (12.5 mM), KI (99.4 mM)

and ammonium molybdate tetrahydrate (0.04 mM). KHP and NaOH provide pH buffering,

while ammonium molybdate catalyzes the reaction.
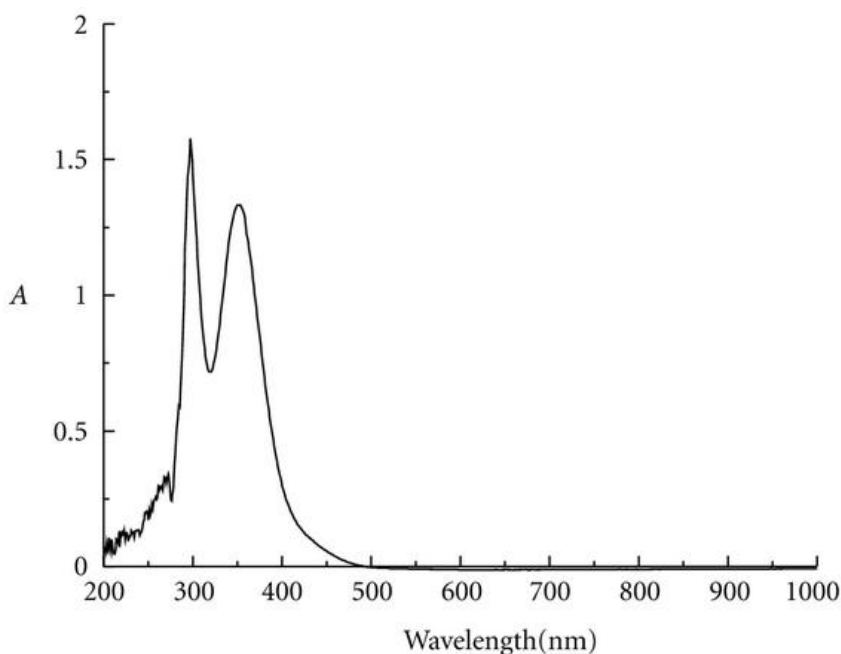
Figure 3.5 UV-Vis Absorbance spectrum of triiodide (adapted from Li et al.[44] with

permission from Hindawi Publishing)

The UV-Vis spectrum for I_3^- (Fig. 3.5) shows absorption peaks at 293 and 351 nm. A

Varian Cary 100 UV-Vis spectrophotometer set to 351 nm wavelength and a quartz cuvette

(Hellma) with 10 mm path length were used for the absorbance measurements. 351 nm was

chosen because at the higher energy (293 nm), the I-I bond may break. Assuming each I

atom uses its p_z orbital as the principle basis in bonding, hν at 351 nm promotes one electron

from the non-bonding (σ_g) molecular orbital to the anti-bonding (σ_u^*) orbital, resulting in a

bond order of 0.25 per each I-I bond. At 293 nm, both electrons in the non-bonding MO are

promoted to the anti-bonding MO, resulting in a bond order of 0.

From the UV-vis absorbance measurements, a calibration curve was determined as follows,

$$[H_2O_2]_{ppm\ (wt)} = \frac{(ABS_{sample} - ABS_{blank}) \times 10}{0.7776 \times S} \qquad (3.4)$$

where S is the sample volume (mL).

The sample pH has significant impact on the measurements. Ovenston and Rees found that the presence of free acid markedly increased the liberation of I_2, even in the blank solution [45]. Therefore, blank measurements were conducted using the fresh electrolyte with the corresponding pH as the sample. This method is sensitive in the $[H_2O_2]$ range of 1 to 15 ppm (wt) without sample dilution.

Chapter 4: Results and Discussions

This thesis project aims to synthesize and investigate a novel redox catalyst for the O_2 electroreduction to H_2O_2. The redox behavior and oxygen reduction catalytic activities of several redox catalysts were compared via cyclic voltammetry and oxygen reduction with the rotating disk-ring electrode in acidic (0.1 M H_2SO_4) and near neutral (0.1 M K_2SO_4) electrolytes. The structure of riboflavinyl-anthraquinone-2-carboxylate ester was analyzed by Fourier transform infrared spectroscopy. Batch H_2O_2 electrosynthesis using the selected redox catalyst was then employed to demonstrate long term catalyst performance and durability.

4.1　Characterization of Riboflavinyl-anthroquinone-2-carboxylate ester (RF-AQ)

The structures of anthraquinone-2-carboxylic acid (CAQ), riboflavin (RF) and riboflavinyl-anthraquinone-2-carboxylate ester (RF-AQ) are shown in Fig. 4.1. The mid IR spectra of CAQ, RF and RF-AQ are presented in Fig. 4.2.

The IR peaks were identified applying the selection rules described by common organic spectroscopic methods and techniques [46-48]. From the IR spectra, the broad peak at about 3330 cm^{-1} (Fig. 4.2b and 4.2c) is due to the O-H stretch of H-bonded alcohol groups observed in both RF and RF-AQ. Peaks at 1730, 1240 and 1080 cm^{-1} (Fig. 4.2c) are generated by one C=O stretch and two C-O stretch modes of an unsaturated ester, which in this case is a characteristic feature of RF-AQ. The peak at about 1720 cm^{-1} observed in Fig. 4.2b is due to the C=O stretch of the ketone groups in RF. This peak in Fig. 4.2c is likely hidden under the more prominent C=O stretch of the ester at 1730 cm^{-1} in the RF-AQ spectrum. Another C=O stretch mode is observed at 1680 cm^{-1} for both RF-AQ (Fig. 4.2c)

and CAQ (Fig. 4.2a), due to the ketone groups of anthraquinone. C-N stretch modes of aromatic amines are observed for both RF-AQ (Fig. 4.2c) and RF (Fig. 4.2b) at about 1270 and 1340 cm^{-1}.
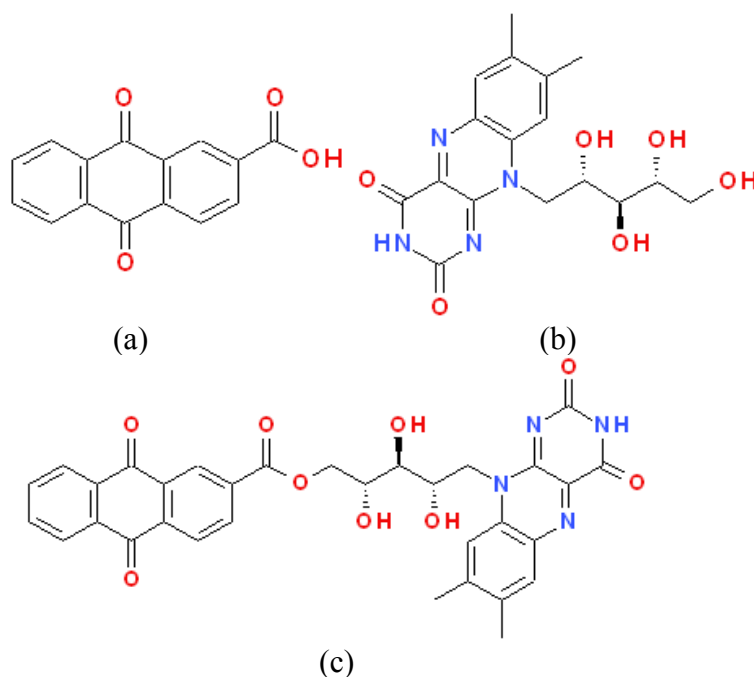
Figure 4.1 Structures of CAQ (a), RF (b), and RF-AQ (c)

The spectral features of CAQ that are unique to the carboxylic acid group (Fig. 4.2a) are not observed in RF-AQ (Fig. 4.2c), validating therefore that the esterification reaction (Eqn. 3.1) with RF has occurred and the RF-AQ product was well purified. Thus, the very broad band between 3400 and 2400 cm^{-1} due to the O-H stretch of carboxylic acid is only observed for CAQ (Fig. 1c). Moreover, the peaks at 1700, 1280 and 930 cm^{-1} representing the stretch modes of C=O, C-O and O-H respectively of the carboxylic acid group, are observed only in the CAQ spectrum (Fig. 4.2c). Thus, the IR analysis supports the structure of RF-AQ shown in Fig. 4.1c.

Appendix A provides further details and guideline for IR absorption band assignments.
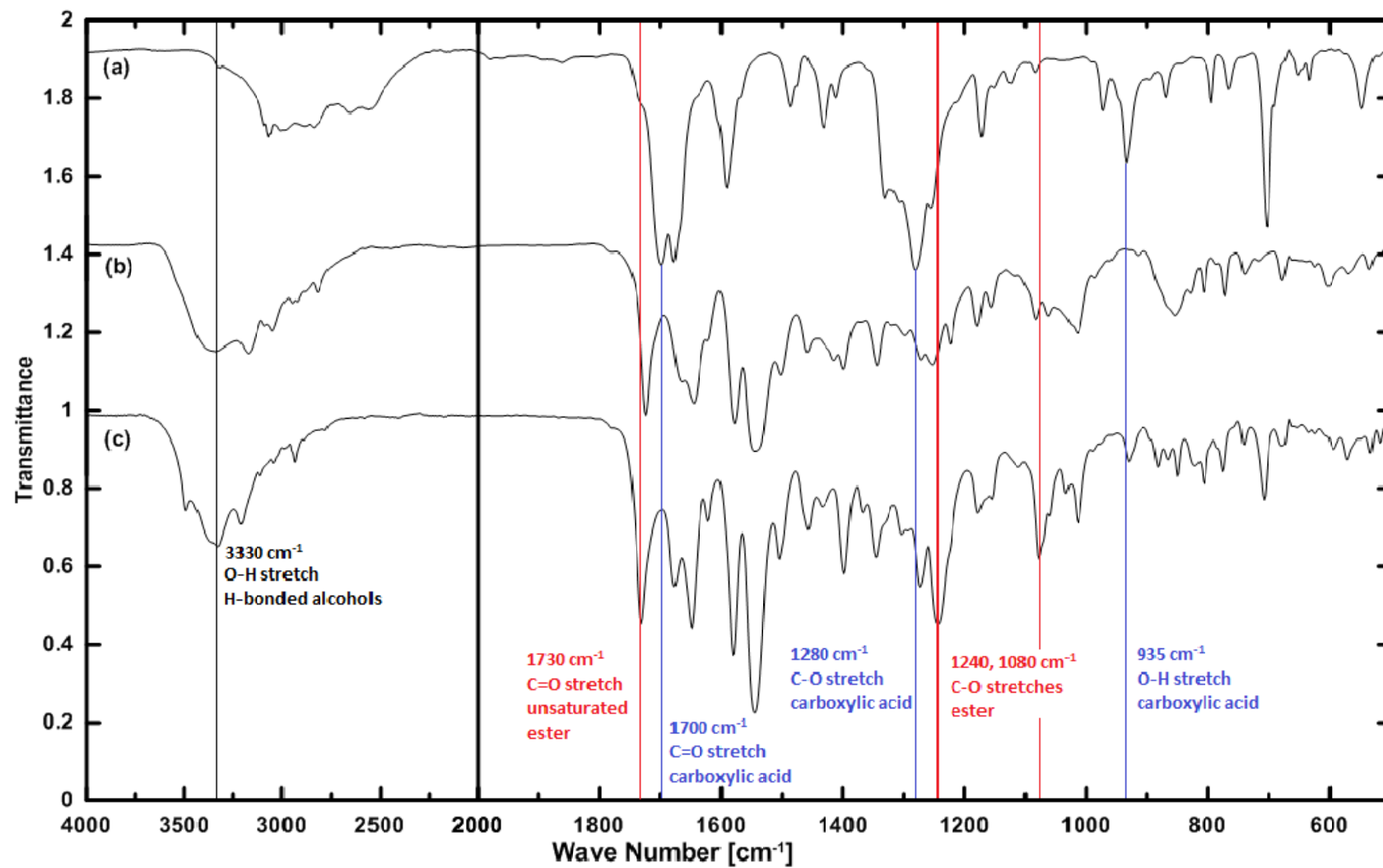
Figure 4.2 Fourier transform infrared Spectra of CAQ (a), RF (b), and RF-AQ (c)

4.2   Catalyst Screening via Cyclic Voltammetry and RRDE

The quinone catalysts listed in Table 3.1 and RF-AQ were examined via cyclic voltammetry in 0.1 M H_2SO_4 and in 0.1 M K_2SO_4.   Oxygen reduction reaction was performed with the RRDE setup presented in Section 3.6.1. The experiments were performed using a catalyst loading of 0.66 mg cm^{-2} on the RRDE tip, at 21°C and 1 bar$_{abs}$ pressure. Results compare the oxygen reduction onset potential and selectivity for H_2O_2.

4.2.1   Oxygen Reduction in 0.1 M K_2SO_4

0.1 M K_2SO_4 was employed to examine the catalytic activity of each redox catalyst in a pH neutral environment. Fig. 4.3 shows the oxygen reduction reaction with the modified electrodes. Fig. 4.3a shows the net Faradaic current due to O_2 electroreduction, after correction for the charging and discharging of the double layer capacitance and the intrinsic catalyst reduction in the absence of O_2 (measurements in N_2-purged electrolyte). Fig. 4.3b presents the oxidation current of H_2O_2 collected at the ring electrode (collection efficiency equal to 38%). The selectivity of the catalysts towards H_2O_2 formation, shown in Fig. 4.3c was calculated from the disk and ring currents as follows [49]:

$$Selectivity = \frac{200 \times I_{ring}}{(N \times |I_{disk}|) + I_{ring}} \qquad (4.1)$$

where N, I_{ring} and I_{disk} refer to the collection efficiency of the ring, ring current, and disk current respectively.

Figure 4.3 Oxygen electroreduction in 0.1M K_2SO_4. (a) O_2 reduction measurements obtained from the rotating disk electrode, (b) ring current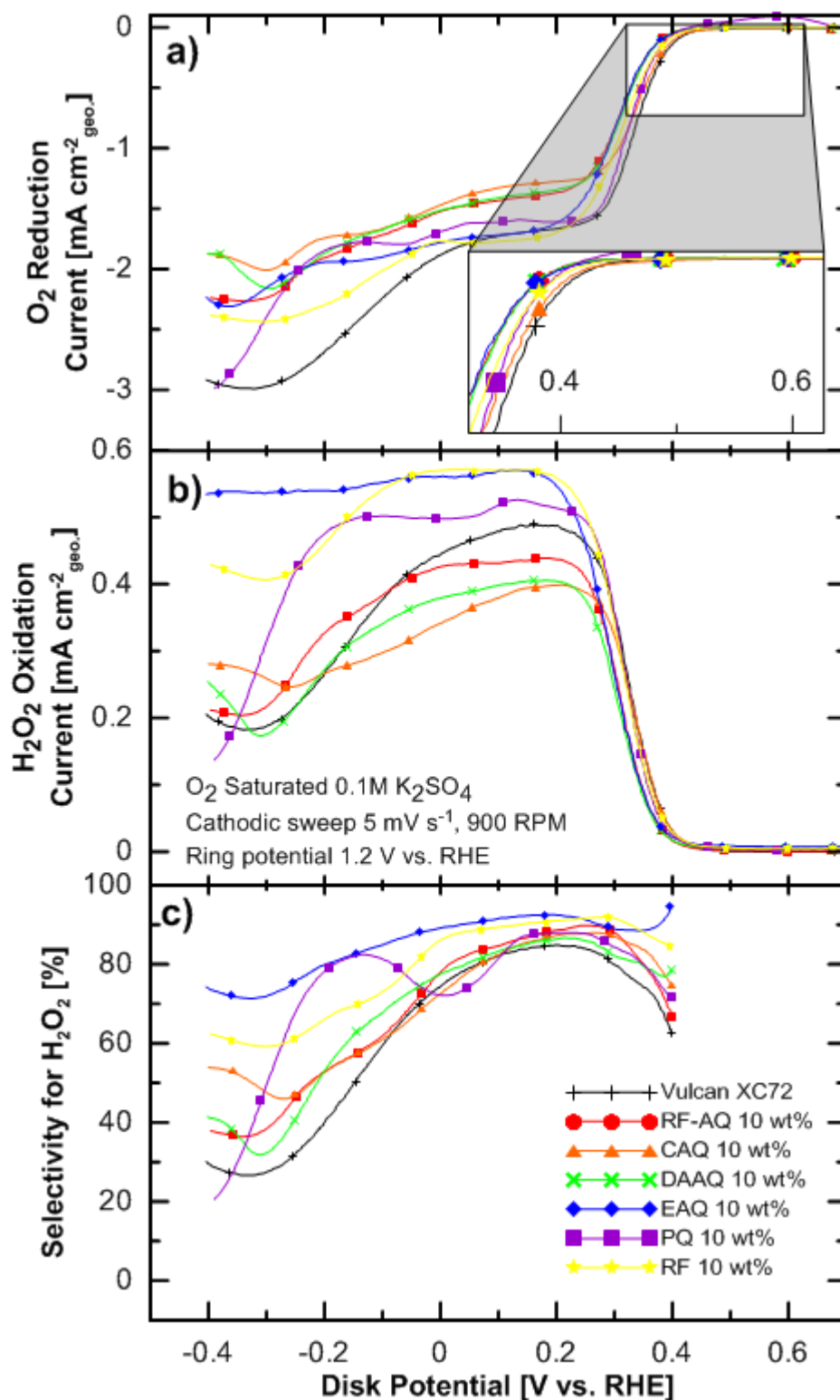 densities, and (c) Selectivity of the catalysts for reduction of O_2 to H_2O_2. The experiments were performed using a catalyst loading of 0.66 mg cm^{-2} on the RRDE tip, at 21°C and 1 bar$_{abs}$ pressure.

It is observed that none of the redox catalysts increased the O_2 reduction onset potential, compared to the Vulcan XC72 carbon baseline. However, modifications with riboflavin (RF 10 wt%), 2-ethyl-anthraquinone (EAQ 10 wt%) and phenanthrenequinone (PQ 10 wt%) increased the selectivity for H_2O_2 in the transport limiting regime near 0.1 V vs. RHE, where the EAQ modified electrode increased the selectivity by 15 ± 5 % compared to Vulcan XC72 (Fig. 4.3c). EAQ also retarded the four electron reduction of O_2. At -0.3 V vs. RHE, the EAQ modified electrode increased the selectivity by 45 ± 5 % compared to Vulcan XC72.

Table 4.1 outlines the reduction potentials of the redox catalysts studied. None of the redox catalysts raised the O_2 reduction potential because their own reduction potentials are much more negative compared to the O_2 reduction onset potential by Vulcan XC72 catalysis (about 0.4 V vs. RHE). Fig. B.1 presents the cyclic voltammograms of each quinone under N_2 purged 0.1 M K_2SO_4 electrolyte. It is also observed that the CVs show strong irreversible behavior.

Table 4.1 Reduction peak potentials of redox catalysts

Species	Peak Reduction Potential (V vs. RHE)
RF-AQ	-0.115
CAQ	-0.242
DAAQ	< -0.4
EAQ	-0.287
PQ	0.035
RF	-0.096

Although O_2 reduction to H_2O_2 in near neutral pH environments has profound significance in biological systems, for the purpose of electrogeneration of H_2O_2 in an engineering setting, the acidic and alkaline media are more dominant. The trickle-bed reactor and the Dow-Huron cell employing alkaline electrolyte were explained in Chapter 2. Fuel

cells (employing H_2, alcohols or carboxylic acids) and electrolysis cells (employing external power supply to break down water).

4.2.2   Oxygen Reduction in Acidic Electrolyte

The commonly used Nafion[®] membrane is a solid acid whose pH can be approximated to be about 1. The catalyst's performance in acidic environment is therefore crucial to its applicability in such electrosynthesis cells. The catalytic activity of each redox catalyst in the acidic environment was examined using 0.1 M H_2SO_4. Fig. 4.4 shows the oxygen reduction reaction with the modified electrodes. The three panels have the same meanings as presented in Fig. 4.3.

The standard potential of oxygen reduction to H_2O_2 is 0.70 V vs. SHE. Modifications of the Vulcan XC72 by RF-AQ (10 wt%) or RF (10 wt%) increased the onset potential of the O_2 reduction to H_2O_2 by up to 100 mV compared to the bare Vulcan XC72 and CAQ, respectively (Fig. 4.4a). Furthermore, for disk electrode potentials between 0.25 V and 0 V the H_2O_2 generation rate was the highest in the case of the RF-AQ catalyst as shown by the higher H_2O_2 oxidation ring current densities (up to 0.5 mA cm^{-2}, Fig. 4.4b) compared to the other catalysts.   For disk electrode potentials below 0.1 V vs. RHE, a selectivity for H_2O_2 of 85 ± 5 % is observed for the RF-AQ catalyst, which is 20% higher than for the baseline Vulcan XC72 (Fig. 4.4c). The H_2O_2 selectivity for the RF-AQ modified electrode, in the potential window between approximately 0.25 to 0.1 V vs. RHE, is lower than that at potentials below 0.1 V because a portion of the cathodic current is spent to reduce the redox catalyst originally in the oxidized form. Below about 0.1 V vs. RHE, all RF-AQ is in the reduced form and thus the true H_2O_2 selectivity is captured in this potential region.

The selectivity is also influenced by the competing secondary reaction, which is the reduction of H_2O_2 to H_2O:

$$H_2O_2 + 2H^+ + 2e^- \rightarrow 2H_2O, \quad E^0_{298K} = 0.53 \text{ V/SHE} \quad\quad (4.2)$$
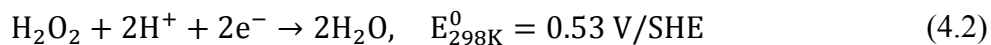
Riboflavin (RF) itself shows pronounced activity towards O_2 reduction to H_2O_2, as well as assistance to the quinone reduction (Fig. 3a-c). The constitutional groups of the redox catalyst have profound impact on the catalyst's activity towards O_2 electroreduction. Among the investigated organic redox catalysts, we found RF-AQ the most active and selective for O_2 reduction to H_2O_2. Therefore it was down selected for further studies.
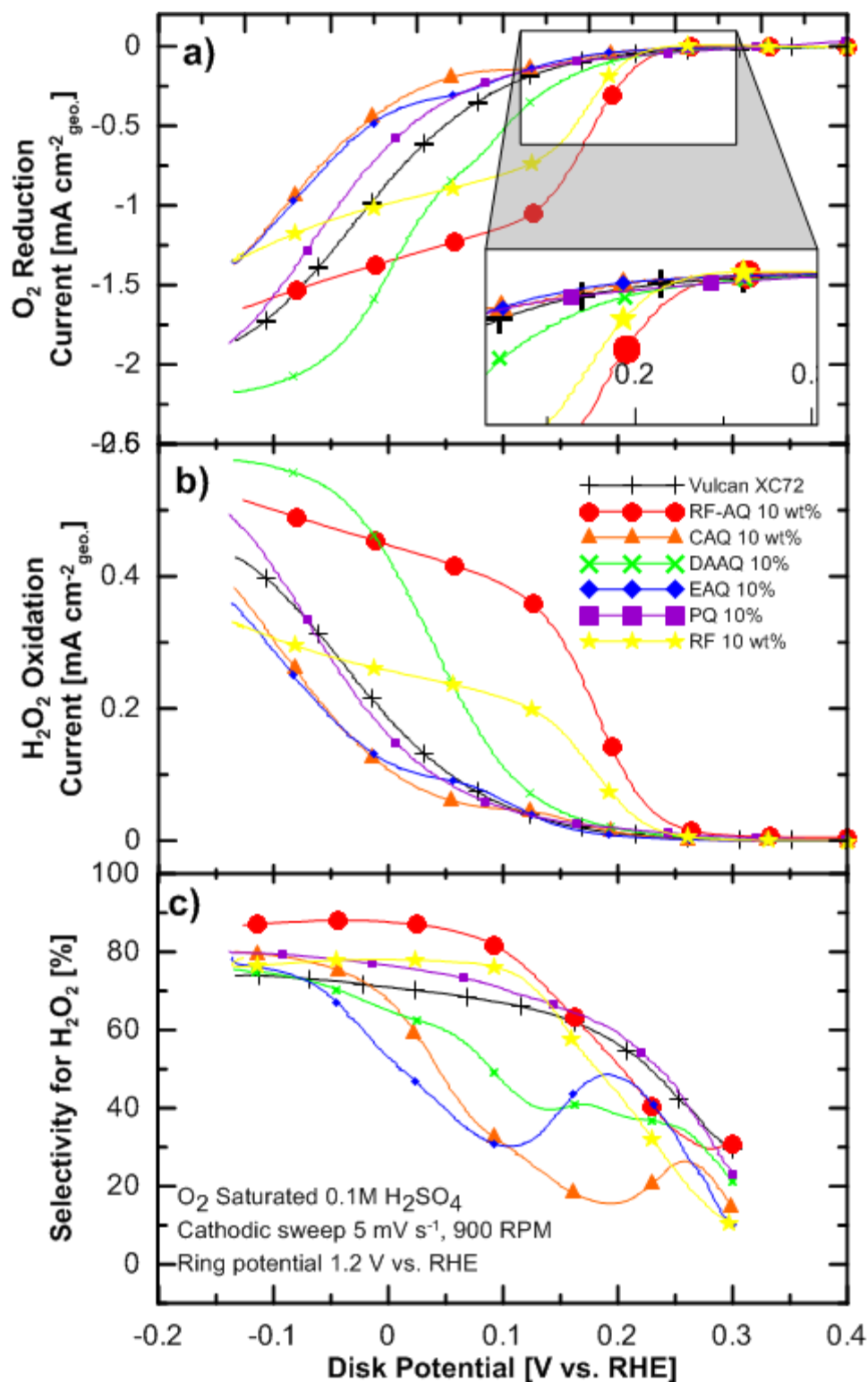
Figure 4.4 Oxygen electroreduction in 0.1M H_2SO_4. (a) O_2 reduction measurements obtained from the rotating disk electrode, (b) ring current densities, and (c) Selectivity of the catalysts for reduction of O_2 to H_2O_2. The experiments were performed using a catalyst loading of 0.66 mg cm^{-2} on the RRDE tip, at 21^oC and 1 bar_{abs} pressure.

4.2.2.1   Redox Behavior of RF-AQ

Figure 4.5 shows the cyclic voltammograms for RF-AQ, in comparison to its constituent fragments – CAQ and RF, on the RRDE electrode, in N_2-purged and O_2-purged 0.1 M H_2SO_4, respectively. The oxygen reduction onset potential defined at -0.1 mA cm^{-2} is about 0.2 V vs. RHE on the bare Vulcan XC72 (Fig. 4.5a). In de-aerated 0.1 M H_2SO_4, the formal redox potential for both RF-AQ (Fig. 4.5b) and RF (Fig. 4.5d) is about 0.2 V whereas for CAQ, it is about 0.15 V (Fig. 4.5c). All the organic redox catalysts are electrochemically active.

Figure 4.5 Cyclic voltammograms for N_2 and O_2 purged cells. (a) Vulcan XC-72, (b) 10 wt% RF-AQ, (c) 10 wt% CAQ, and (d) 10 wt% RF. The experiments were performed using a catalyst loading of 0.66 mg cm^{-2} on the RRDE tip, 0.1 M H_2SO_4 electrolyte, at $21^{o}C$ and 1 bar_{abs} pressure.

It was observed that RF (molecular weight 376 g mol^{-1}) showed a lower reduction peak current density than CAQ (MW 252 g mol^{-1}) in the de-aerated electrolyte, for the same loading on a weight basis. It was also observed t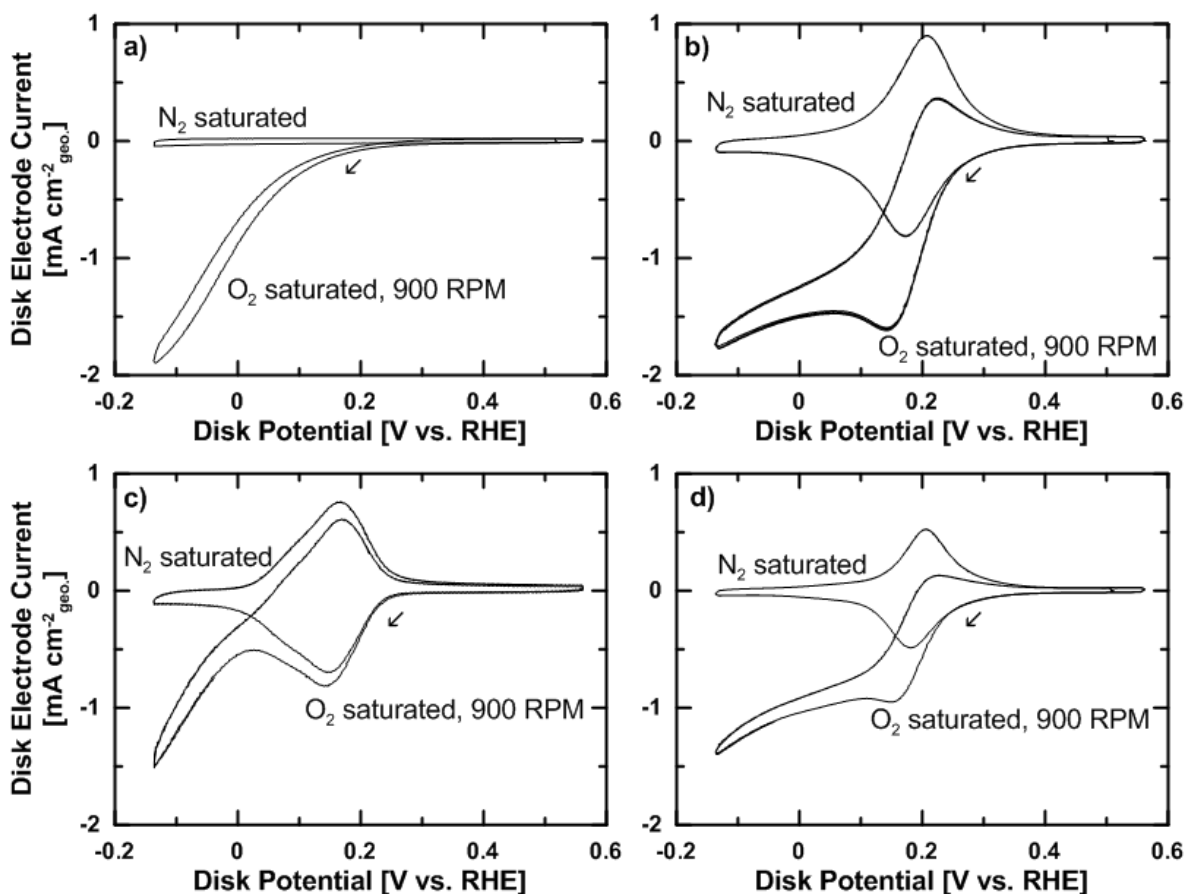hat RF-AQ (MW 610 g mol^{-1}) with a much lower molar loading showed almost as large a reduction peak current density as CAQ; however, its reduction peak potential was the same as that of RF. This could be attributed to the reduction of the RF constituent in RF-AQ, and subsequently mediating the reduction of the AQ constituent.

In the O_2-saturated electrolyte all three catalysts generated reduction peaks at potentials virtually equal to the characteristic catalyst reduction peak potential in the absence of O_2. The corresponding reduction peak current densities are composed of two electrode reactions: net O_2 electroreduction and redox catalyst electroreduction, respectively (Fig. 4.5b-d). RF-AQ generated the highest reduction peak current density, -1.6 mA cm^{-2} followed by RF with -1 mA cm^{-2} and lastly CAQ with -0.75 mA cm^{-2}. The deviation of the reduction waves in the presence of O_2 from the reduction waves in the absence of O_2 suggests the turn-over frequencies of the redox catalysis. RF-AQ showed considerably greater deviation than RF and CAQ. Its reduced form reacts readily with O_2.

4.2.2.2   Effect of Catalyst Loading and Nafion® Content in the Catalyst Layer

The effects of loadings of the redox catalyst and the Nafion® content were examined by cyclic voltammetry via the RRDE technique. Fig. 4.6 shows the oxygen reduction reaction for the modified electrode with varying RF-AQ content (0, 5 and 10 wt%) and Nafion® contents of 0.09, 0.18 and 0.3 mg cm$^{-2}_{geo}$. The electrodes modified with RF-AQ 10 wt% and with RF-AQ 5 wt% generated H_2O_2 with comparable selectivity (Fig. 4.6c); however the higher loading produced more H_2O_2 in quantity (Fig. 4.6b). The Nafion® content is observed

to have the most significant impact on the selectivity of H_2O_2 formation (Fig. 4.6c). The electrode with a Nafion® loading of 0.09 mg cm$^{-2}_{geo}$ generated H_2O_2 with about 20 ± 5 % lower selectivity at 0 V vs. RHE compared to the electrodes with Nafion® loadings of 0.18 and 0.3 mg cm$^{-2}_{geo}$, which are comparable. The higher Nafion® loadings may have increased the hydrophilicity of the thin electrode layer, and thus was beneficial to the transport of the $H_2O_{2(aq)}$ from being further reduced to H_2O.
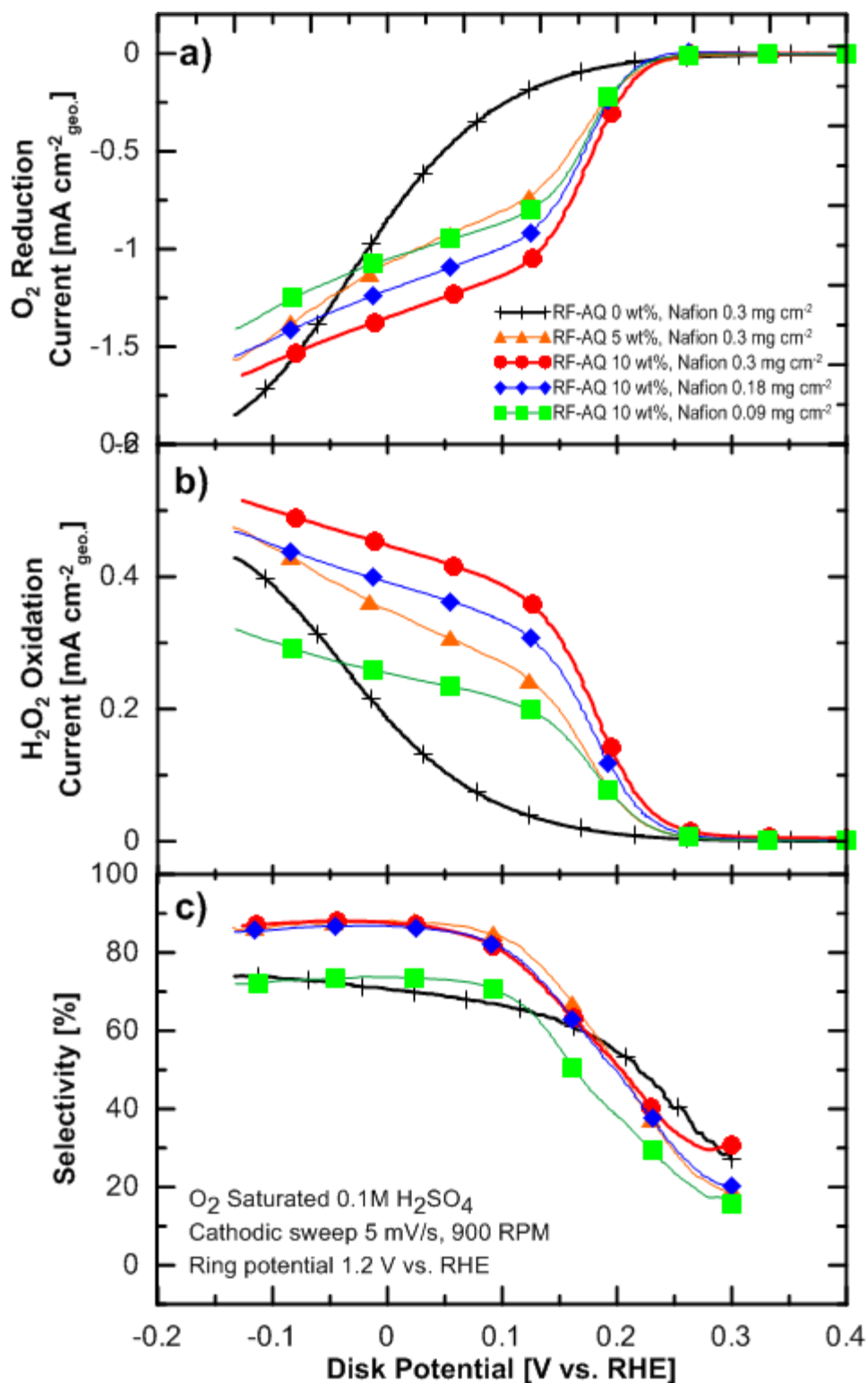
Figure 4.6 Oxygen electroreduction and the effects of RF-AQ and Nafion® content in 0.1 M H_2SO_4. (a) O_2 reduction measurements obtained from the rotating disk electrode, (b) ring current densities, and (c) Selectivity of the catalysts for reduction of O_2 to H_2O_2. The experiments were performed at 21°C and 1 bar$_{abs}$ pressure.

4.3 Reaction Mechanism of O_2 Electroreduction to H_2O_2 via RF-AQ Catalysis

Figure 4.7a shows cyclic voltammograms as a function of sweep rate, recorded in N_2-saturated 0.1 M H_2SO_4 electrolyte using the 10 wt% RF-AQ catalyst deposited onto the RRDE GC tip with an effective RF-AQ coverage of 1.07 x 10^{-7} mol cm^{-2}_{geo} (calculated from the composite catalyst composition). A reversible wave is observed with a formal redox potential at 0.2 V vs. RHE. The reduction peak current density was a linear function of the potential sweep rate (Fig. 4.7b). Thus, assuming Nernstian behavior of the surface modified electrode, the number of electrons can be estimated from the peak current densities, as expressed in Eqn 2.21:

$$i_p = \frac{1000n^2F^2v\Gamma^*_{RF-AQ}}{4RT} \qquad (4.3)$$

where n, v, A and Γ^*_{RF-AQ} represent the number of electrons transferred, potential sweep rate, geometric area of the electrode, and the coverage of RF-AQ, respectively.

The one electron reduction of RF-AQ in the N_2-purged electrolyte raises the question whether the anthraquinone structural unit or the riboflavin constituent participate in the electroreduction and mediation of the O_2 reduction. It is evident that RF has a pronounced effect in the mediated O_2 reduction reaction (Fig. 4.5d). The mechanism by which the anthraquinone constituent improved the H_2O_2 yield and selectivity (Fig. 4.4b-c) is unknown and deserves further investigation.
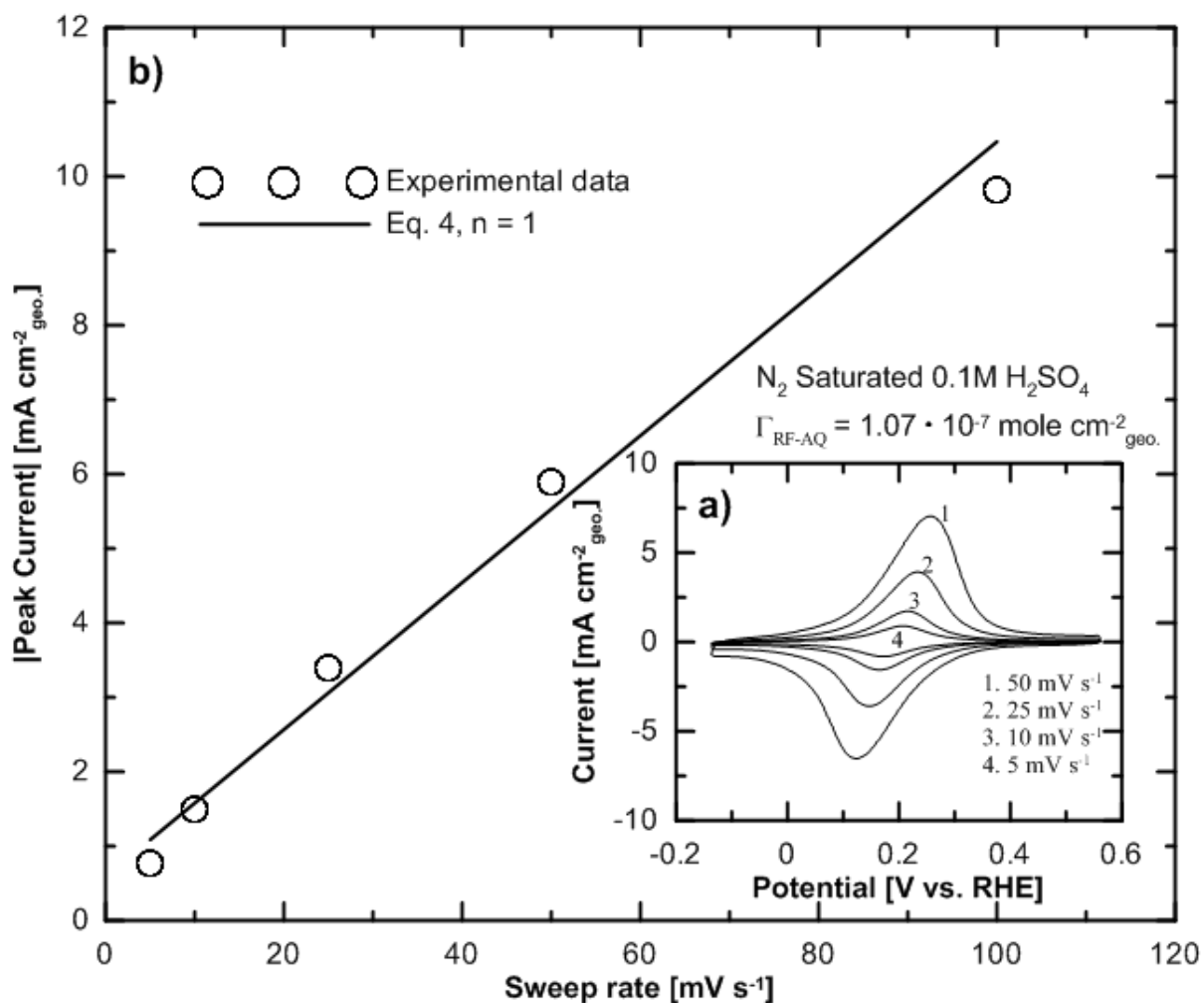
Figure 4.7 RF-AQ redox waves with 10 wt% RF-AQ loading. (a) redox waves of the RF-AQ couple, and (b) averaged peak current density as a function of potential sweep rate. The experiments were performed using a catalyst loading of 0.66 mg cm^{-2} on the RRDE tip, 0.1 M H$_2$SO$_4$ electrolyte, at 21 $^{\circ}$C and 1 bar$_{abs}$ pressure.

A reaction scheme for the mediated O$_2$ reduction is proposed in Figure 4.8, where the semi radicals (b or c) formed by the one-electron reduction of RF (a) is responsible for the electrocatalytic activity for O$_2$ reduction, as supported by reports of mediatied O$_2$ reduction by many quinoid compounds [50]. The radicals (b or c), stabilized by a number of resonant structures, react thermochemically with O$_2$ to form peroxyl radical adducts (d or e). The formation of the adducts has been proposed as the rate determining step [7, 50]. H$_2$O$_2$ is

thereafter formed via the subsequent electro-reduction of adduct (d or e) to adduct (f) followed by its molecular rearrangement with simultaneous regeneration of the riboflavin structural unit (referred to also as redox mediation).

Riboflavin has been reported to assist the reduction of quinones [35, 36]. In the present study, it is evident that the RF structural unit is active for the 2e⁻ O_2 reduction in the RF-AQ catalyst. The molecular and electronic interaction between RF and AQ is unknown at present.
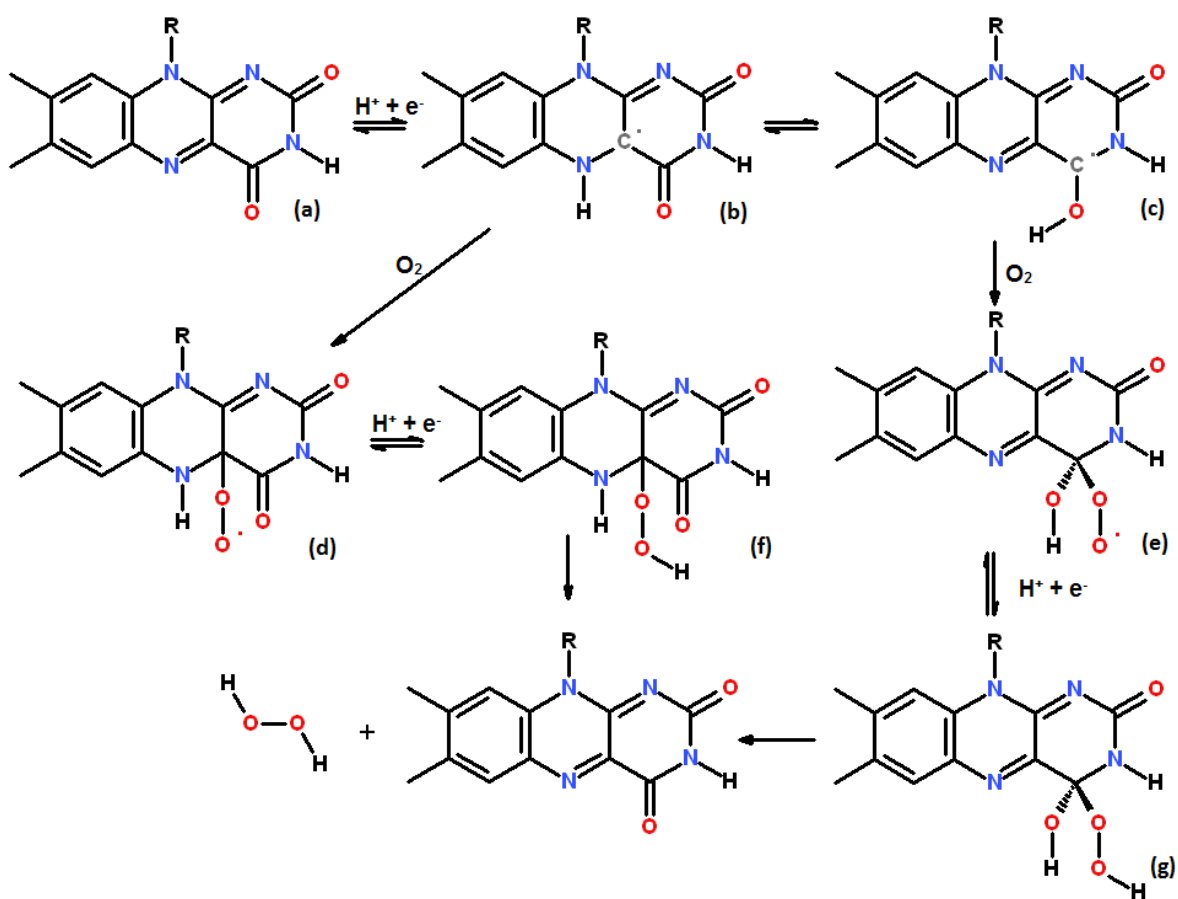
Figure 4.8 Proposed reaction scheme of RF-AQ reduction and mediated O_2 reduction to H_2O_2

From the RRDE experiments of the RF-AQ modified Vulcan XC72 carbon with 5 and 10 wt% RF-AQ contents, and the unmodified Vulcan XC72 catalysts at rotation speeds of 100, 400, 900 and 1200 RPM, the Koutecky-Levich relationship at 0.1 V vs. RHE was generated and it is shown in Figure 4.9 [51]:

$$\frac{1}{i_F} = \frac{1}{i_k} + \frac{1}{i_{dl}} = -\frac{1}{1000nFkC_{O_2,b}} - \frac{1}{620nFD_{O_2}^{2/3}\nu^{-1/6}C_{O_2,b}\omega^{1/2}} \qquad (4.4)$$

where j_F, j_k, j_{dl}, k, C_b, F, D, n, ν and ω represent the total Faradaic current density, kinetic current density, diffusion limited current density, electrochemical rate constant for O_2 reduction, bulk concentration of the analyte (dissolved oxygen), Faraday's constant, diffusivity of the analyte, number of electrons transferred, viscosity of the electrolyte, and angular velocity of the rotating electrode, respectively.
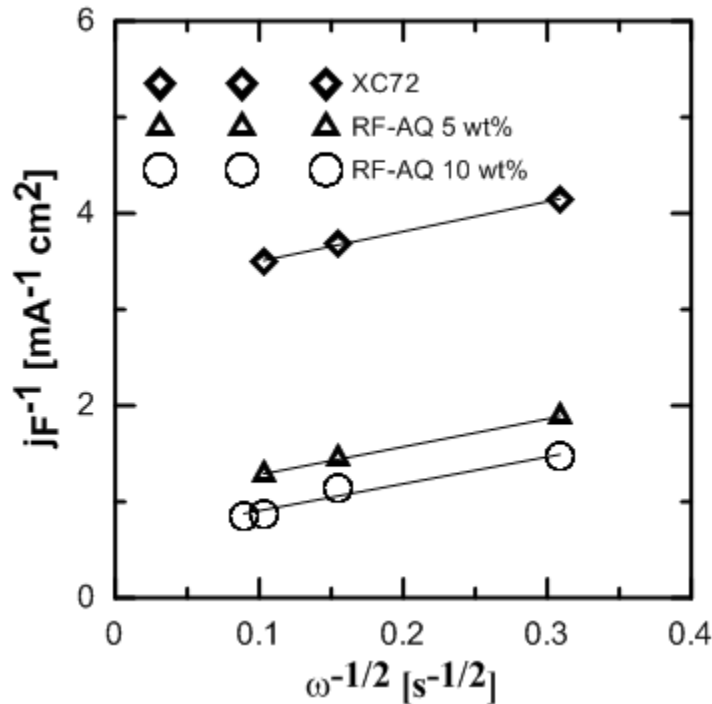
Figure 4.9 Koutecky-Levich plot for O_2 reduction on the unmodified Vulcan XC72, 5 wt% and 10 wt% RF-AQ on Vulcan XC72 catalysts. The experiments were performed using a catalyst loading of 0.66 mg cm^{-2}, 0.1 M H_2SO_4 electrolyte, at 21°C and 1 bar$_{abs}$ pressure.

Using the literature reported values of $C_{O2,b} = 1.26 \times 10^{-6}$ mol cm^{-3}, $D_{O2} = 1.93 \times 10^{-5}$ cm^2 s^{-1}, and $\nu = 1.009 \times 10^{-2}$ cm^2 s^{-1} [7], and the reciprocal of the slopes in Figure 4.9, n is estimated to be about 2, confirming the two electron reduction of O_2 mediated by the catalysts. From the reciprocal intercept of the Koutecky-Levich plots, the electrochemical rate constants (at 0.1 V vs. RHE) are estimated to be 1.51×10^{-6}, 4.53×10^{-6}, and 6.91×10^{-6} cm s^{-1} for the Vulcan XC72 carbon baseline, 5 wt% RF-AQ modified Vulcan XC72, and 10 wt% RF-AQ modified Vulcan XC72 catalysts, respectively. Thus, the RF-AQ modification significantly improved the kinetics of O_2 reduction to H_2O_2.

4.4   Adhesion and Monolayer Coverage of RF-AQ on Vulcan XC-72

The adhesion of RF-AQ to Vulcan XC72 and the RF-AQ/ Vulcan XC72 catalyst to the GC disk were examined by comparing the cyclic voltammograms recorded in the N_2 purged electrolyte before and after performing the oxygen reduction experiments. The redox waves of the immobilized RF-AQ showed no decrease in peaks, suggesting good adhesion to the GC tip of the RRDE during the entire time of the O_2 reduction measurements. Furthermore, the ORR voltammograms were also stable for several cycles (Fig. 4.10). The immobilization is attributed to the π-π interaction between the polycyclic aromatics and the carbon support [52].

To approximate the maximum RF-AQ loading on the carbon support for complete monolayer coverage, the molecular volume of RF-AQ was estimated by total energy minimization in vacuum to be 685 Å^3. A trial version of CambridgeSoft ChemBio 3D software was used to perform the computation using the Hartree-Fock method with the Gaussian algorithm and 6-31G basis set [40, 41]. For comparison, a van der Waals volume of

504 Å^3 was calculated from the correlation developed by Zhao et al. [53], which is about 25 %

less than that predicted by the computational chemistry method. The correlation developed

by Zhao et al. assumes the atoms and bonds present in the molecule are rigid, whereas the

Hartree-Fock method allows the molecule to relax to an energetic minimum.

Assuming the active surface area of the Vulcan XC72 powder substrate is 200 $\text{m}^2\ \text{g}^{-1}$

from N_2 adsorption isotherms [42], and that the RF-AQ molecules are rigid spheres with a

volume estimated by the computational chemistry method, the complete RF-AQ monolayer

coverage of Vulcan XC72 is estimated to occur at an RF-AQ loading of 17.7 wt%. This

treatment is limited as it does not consider the molecular shape and orientation of RF-AQ

over the carbon substrate. However, it provides a good guideline to the monolayer saturation.

Figure 4.10 shows the cyclic voltammograms for modified electrodes with 10 wt%

RF-AQ loading (a) and 15 wt% RF-AQ loading (b) for the first and 50th cycle at a potential

scan rate of 5 mV s^{-1}. Fig. 4.10a shows no significant decrease in the redox peaks after about

2.3 hours; whereas Fig. 4.10b shows a decrease in the redox waves approaching that of
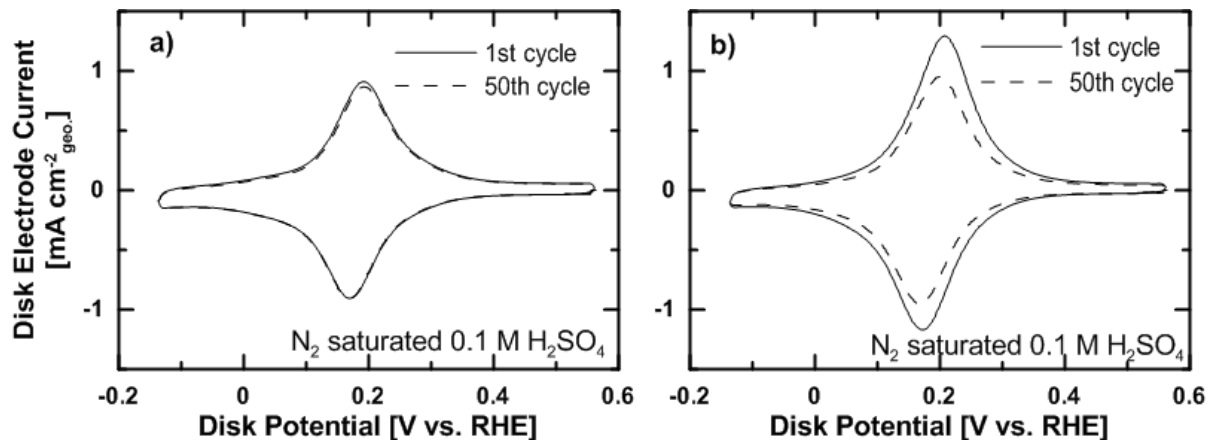
Fig. 4.10a.

Figure 4.10 CVs for electrodes using Vulcan XC72 modified with 10 (a) and 15 (b) wt%
adsorbed RF-AQ. The experiments were performed using 0.1 M H_2SO_4 electrolyte, at 21°C
and 1 bar_{abs} pressure.

As the RF-AQ loading approaches monolayer saturation on the Vulcan XC72 carbon surface, the satability of the adsorbed RF-AQ diminishes, and its desorption is evident.

4.5   Chronoamperometric Batch H_2O_2 Electrosynthesis

Figure 4.11 shows the H_2O_2 generation and current efficiency of the Vulcan XC72 carbon baseline and a number of RF-AQ modified Vulcan XC72 catalyst in the electrolysis cell described in Section 3.6.2 using O_2 purged 0.5 M H_2SO_4. The cathode potential was kept constant at 0.1 V vs. RHE. The H_2O_2 generation is expressed both as accumulative concentration in weight-based parts per million (ppm) and in molar quantities normalized by the electrode's geometric surface area ($\mu mol\ cm^{-2}_{geo.}$).   The catholyte volume was kept constant (136 ml) throughout the electrolysis experiments, such that the two y-axes correspond in value.

The RF-AQ modification improved both the H_2O_2 generation and the current efficiency. With a total composite catalyst loading of $2.50 \pm 0.05\ mg\ cm^{-2}_{geo}$ (10 wt% RF-AQ, Vulcan XC-72 and Nafion) on the Toray$^{®}$ carbon paper, 432 ppm H_2O_2 was produced at 21 ^{o}C with 70 ± 5 % average current efficiency after 24 hours. The initial H_2O_2 production rate was 21 $\mu mol\ hr^{-1}\ cm_{geo}^{-2}$ during the first two hours. For the unmodified Vulcan XC72 only about 170 ppm H_2O_2 was produced at 21 ^{o}C with 55 ± 5 % current efficiency after 24 hours (Fig. 4.11 a and c). A higher total composite catalyst loading of 3.40 mg $cm^{-2}_{geo.}$ produced about 500 ppm of H_2O_2 after 24 hours, but with about 10 % lower efficiency. This lower efficiency was likely due to the thicker porous catalyst layer retaining the generated H_2O_2, which subsequently underwent further reduction to H_2O.

The elevated temperature of 50 ^{o}C considerably improved the H_2O_2 production rate of the RF-AQ redox catalyst, by increasing the rate of the limiting thermochemical reaction of

the HRF-OO* adduct formation (Fig. 4.8 c or d). A much higher H_2O_2 concentration, 628 ppm (wt) after 24 hours, was achieved but at this temperature H_2O_2 decomposition was also significant as shown by the drop of the apparent current efficiency from 80 ± 5 % initially to about 60 ± 5 % after 24 hrs. at 50 ^{0}C (Fig. 4.11 a and c). The effect of temperature on the Vulcan XC72 catalyst was much less pronounced, and the H_2O_2 concentration was below 200 ppm after 24 hrs. The current densities for all electrolysis experiments were stable at both 21 and 50 ^{0}C, and no noticeable desorption of the immobilized RF-AQ was observed during the 24 hour experiments.

Chronopotentiometry experiments also support the findings above. Fig. C.1 shows the same batch electrolysis using a total composite catalyst loading of 2.0 ± 0.05 mg cm$^{-2}_{geo}$ on the Toray$^®$ carbon paper, at 0.25 and 1.0 mA cm^{-2} at 21 and 50 ^{o}C. At 1 mA cm^{-2}, RF-AQ modification increased the H_2O_2 production by over 100 ppm (Fig. C.1c), lowered the potential loss by over 100 mV (Fig. C.1b), and improved the current efficiency by about 30% (Fig. C.1a).
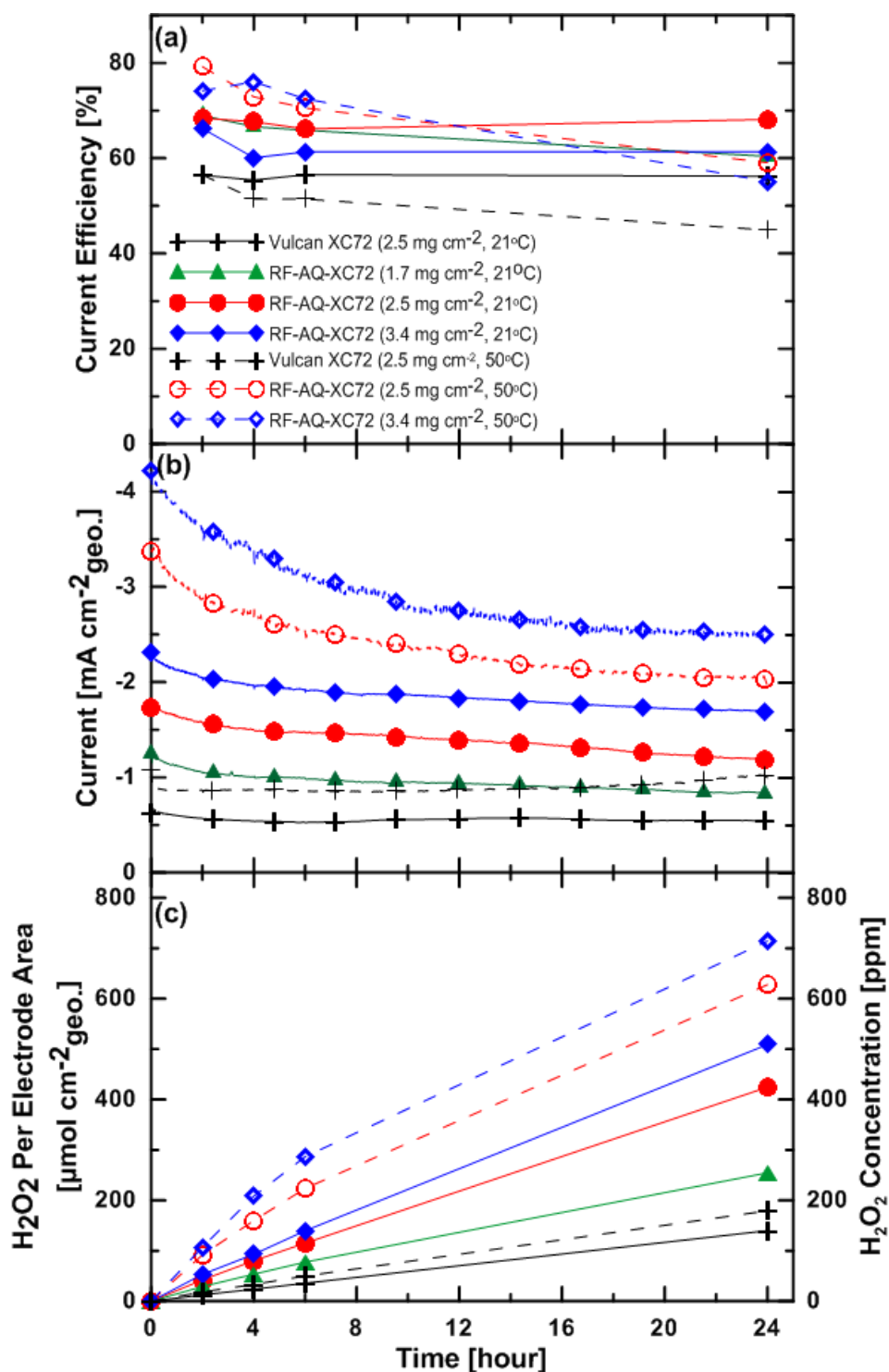
Figure 4.11 Effect of the RF-AQ redox catalyst on H_2O_2 generation in a batch electrolysis cell. (a) Current efficiency of H_2O_2 generation. (b) Cathodic current density, and (c) H_2O_2 accumulative production normalized by the electrode surface area and H_2O_2 concentration as a function of time. The experiments were performed using RF-AQ 10 wt% on Vulcan XC72 carbon, 0.5 M H_2SO_4 electrolyte, at 0.1 V vs. RHE, 1 bar$_{abs}$ pressure and 21°C or 50°C as specified.

4.6   Hydrogen Peroxide Stability in Aqueous Solutions

The thermochemical stability of H_2O_2 was examined over the pH range of 0 to 10 at 295 K. Fig. 4.12 presents the concentration profiles of a commercially available H_2O_2 diluted to about 350 ppm in different pH solutions for 7 days. For pH less than 8, no significant decrease in the H_2O_2 concentration was observed over the 7 day period.
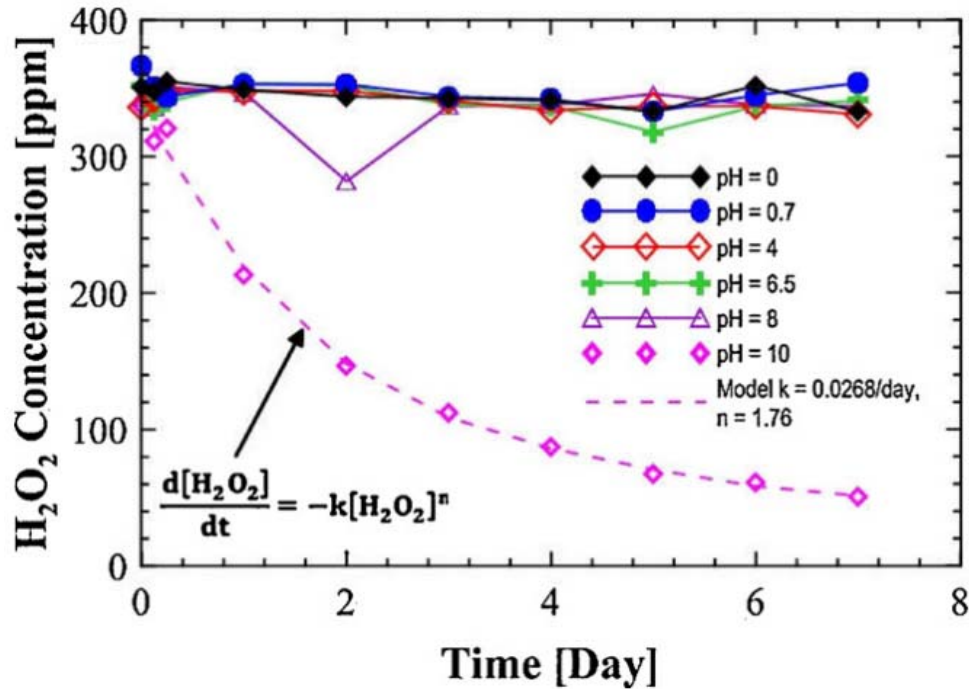
Figure 4.12 Thermochemical stability of H_2O_2 in different pH media at 295 K
using pH 0: H_2SO_4, and pH 0.7 to 10: 0.1 M mono- and di-potassium phosphate buffer
(adapted from Bonakdarpour et al.[22] with permission from Elsevier)

At pH 10, H_2O_2 was observed to decompose with a nth order reaction rate, where n = 1.76. A model kinetic rate can be expressed as the following equation,

$$\frac{d[H_2O_2]}{dt} = -k_{H_2O_2}\, C_{H_2O_2}^n \tag{4.5}$$

where the kinetic rate constant, k_{H2O2}, and order of reaction, n, are determined to be 0.027 ppm(wt) day^{-1} and 1.76 respectively, and C_{H2O2} is the H_2O_2 concentration in ppm(wt).

Hydrogen peroxide stability under alkaline solutions has been studied particularly in the pulp and paper industry. Lee et al. identified that H_2O_2 is sensitive to bicarbonate ions, and thus is very unstable in Na_2CO_3 and $NaHCO_3$ solutions compared to in NaOH solutions. Fig. 4.13 shows accelerated peroxide decomposition at 70 °C in NaOH (pH 13), Na_2CO_3 (pH 11.1) and $NaHCO_3$ (pH 9.2). It is likely that the bicarbonate peranion reacts with H_2O_2 to generate H_2O.
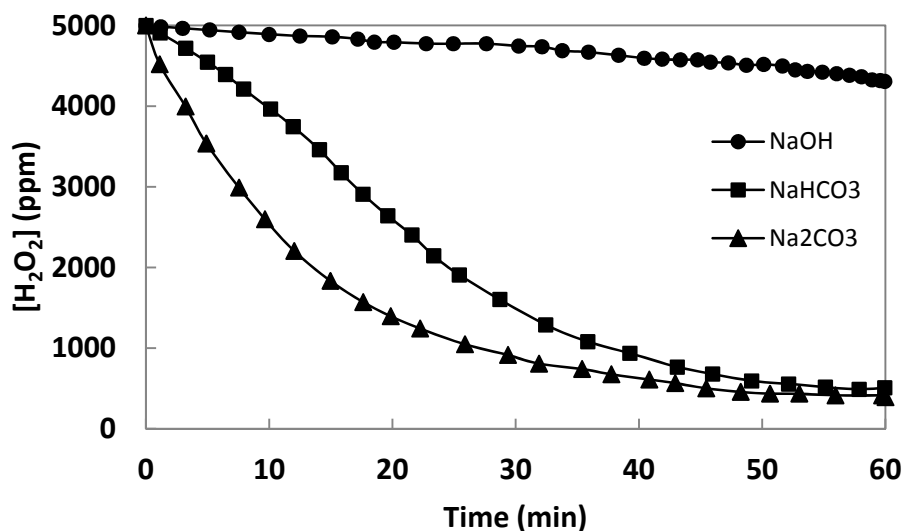
Figure 4.13 Stability of alkaline peroxide at 70 °C in NaOH (pH 13), Na_2CO_3 (pH 11.1) and $NaHCO_3$ (pH 9.2) (adapted from Lee et al.[54] with permission from the Technical Association of the Pulp and Paper Industry)

H_2O_2 synthesis processes utilizing acid media are intrinsically beneficial compared to the H_2O_2 trickle bed reactor or the Dow-Huron cell which employ highly alkaline media, where H_2O_2 decomposition is severe.

Chapter 5: Conclusions and Recommendations

This thesis research reports the synthesis of a novel riboflavinyl-anthraquinone compound which shows electroactive behavior immobilized on a carbon support, and redox catalytic activity for O_2 reduction to H_2O_2 in acidic media. Cyclic voltammetry with a rotating ring-disk electrode assembly was employed to characterize the catalyst. Chromoamperommetry experiments, with the cathode held at 0.1 V vs. RHE, in a batch electrolysis cell were performed up to 24 hours to demonstrate long term H_2O_2 synthesis.

Among the various derivatives of AQ and RF compounds studied in this thesis project, the synthesized RF-AQ compound supported on Vulcan XC72 carbon showed the highest (followed by RF) electrocatalytic activity for O_2 reduction to H_2O_2. RF-AQ at 10 wt% content showed irreversible adsorption over the Vulcan XC72 carbon support, which was estimated to be equivalent to a surface coverage of 0.56. Full monolayer of RF-AQ coverage is estimated at 17.7 wt% loading on Vulcan XC72.

The RF-AQ modified electrode had a 2e⁻ O_2 electroreduction rate constant of 6.9 x 10^{-6} cm s^{-1} (at 0.1 V vs. RHE, 21°C and 1 bar$_{abs}$). Batch electrolysis using a composite catalyst loading of 2.5 mg cm^{-2}, with dissolved O_2 in 0.5 M H_2SO_4 at 21°C and 1 bar$_{abs}$, produced H_2O_2 at an initial rate of about 21 μmole cm$_{geo}^{-2}$ hr^{-1} with current efficiencies up to 70 % at a constant cathode potential of 0.1 V vs. RHE. Electrolysis using the same composite catalyst loading, at 50 $^{\circ}$C promoted the thermochemical step of the mediated O_2 reduction reaction and produced H_2O_2 at an initial rate of 46 μmole cm$_{geo}^{-2}$ hr^{-1} with about 75 % current efficiency under the same potentiostatic conditions. However, at 50 $^{\circ}$C when the H_2O_2 concentration exceeded 200 ppm (wt), the apparent current efficiency dropped

below 70%. This loss in apparent current efficiency, observed at 50 $^{\circ}$C but not at 21 $^{\circ}$C, may be primarily due to H_2O_2 disproportionation.

The identified redox catalyst RF-AQ is a potential cathode catalyst and shows promise in small scale synthesis of H_2O_2 for applications in drinking water treatment facilities employing advanced oxidation processes.

The work presented in this thesis project involves fundamental electrochemical characterization and bench-scale demonstration for H_2O_2 electrosynthesis. Larger scale electrosynthesis cell (eg. Solid polymer electrolyte cell) testing of the synthesized riboflavinyl-anthraquinone-2-carboxylate ester redox catalyst is the most logical continuation of the present work.

5.1   Recommendations

The specific application of generating H_2O_2 to supply drinking water treatment processes requires a significant amount of the chemical commodity, despite only 5 to 10 ppm(wt) is required in the AOP water treatment process.   Based on a small community consuming 500L of potable water per day, about 2.5 kg of H_2O_2 is required.   An appropriate approach is to produce a concentrated H_2O_2 stock solution, which would be added to the inlet stream of the AOP reactor accordingly.

Assuming a continuous process, operated at 50°C, where the current efficiency is at 75 ± 5 %, the current density at 250 mA cm^{-2} (100 times that of the aqueous batch cell, after effective reactor design), and the H_2O_2 production rate at 4.6 mmol cm^{-2} hr^{-1} (100 times that of the aqueous batch cell), it would require about 670 cm^2 (or 0.067 m^2) of electrode

geometric area to satisfy the H_2O_2 demand. Economics of this process and of the direct purchase and transportation of H_2O_2 should be compared to determine its feasibility.

It is recommended that future work emphasizes the optimization and design of the electrosynthesis cell to examine the catalyst durability and effect of temperature on the coupled electrochemical-thermochemical system. The present work employs aqueous cells with the cathode completely immersed in the catholyte saturated with dissolved O_2. Diffusion limiting current was determined to be 10^5 times more severe than the kinetic limiting current. Effective O_2 transport is crucial in the scale up of the electrochemical cell. The following recommendations for O_2 transport optimization is suggested:

1. Three-phase cathode catalyst layer involving effective gaseous O_2 transport and $H^+_{(aq)}$ diffusion to the catalytic sites. Transport of the product H_2O_2 away from the catalyst layer is also necessary to prevent its decomposition in a reductive enrironment. Balance between hydrophobicity and hydrophilicity in the cathode catalyst layer by incorporating Nafion® and PTFE.

2. O_2 pressure at the cathode determines its reactivity. The mechanical stability of the catalyst layer and the electrochemical cell must also be maintained.

3. Temperature has been shown to significantly impact the thermochemical step in the RF-AQ redox catalyzed O_2 reduction to H_2O_2. Operating temperature could be optimized to increase H_2O_2 production while maintaining mechanical stability of the catalyst layer and avoiding RF-AQ desorption from the carbon support. A semi-batch operation may be appropriate for the temperature-dynamic operating condition (non-steady state)

4. Integrating quinone-based catalyst with organo-Co based catalyst in a creative multi-zone catalyst layer could also increase H_2O_2 generation and current efficiency.

5. Water management to the cathode catalyst layer will help the transport of H^+ to the catalyst sites, and the product H_2O_2 away from the catalyst layer.

The reaction pathway for the RF-AQ mediated O_2 reduction is not yet fully tunderstood. To fundamentally study the reaction pathway for the process, the following recommendations are suggested:

1. The in-situ FTIR technique may be applied using a monolayer of RF-AQ adsorbed over an Au thin film grown on a Si prism. Cyclic voltammetry could be applied while time-resolved IR spectra could be used to determine intermediate species generated.

2. Theoretically, computational methods such as the density functional theory (DFT) may be applied to determine the binding energy of the RF-AQ molecules over the graphite substrate. DFT is a suitable method as the system is highly conjugated, and the graphite substrate is a pseudo-metal.

3. DFT could be used to determine sites for H^+ adsorption on the RF-AQ molecule. The subsequent O_2 adsorption and the energetic barrier for H_2O_2 formation could also be determined. Comparison with the reaction intermediate species determined from in-situ FTIR could lead to better understanding of how to functionalize quinone-based catalysts for the purpose of O_2 reduction.

References

1. *Environment Canada: Water - Frequently Asked Questions.* 2011 [cited 2011 November]; Available from: http://ec.gc.ca/eau-water/default.asp?lang=En&n=1C100657-1.

2. O'Connor, D.R., *Report of the Walkerton Inquiry: The Events of May 2000 and Related Issues.* Vol. 1. 2002, Toronto: Ontario Ministry of the Attorney General.

3. *Drinking Water and Wastewater: First Nations, Inuit and Aboriginal Health.* 2011 [cited 2011 November]; Available from: http://www.hc-sc.gc.ca/fniah-spnia/promotion/public-publique/water-eau-eng.php.

4. Parsons, S., *Advanced Oxidation Processes For Water and Wastewater Treatment.* 2005, New York: Iwa Publishing.

5. Vogelpohl, A., *Oxidation Technologies for Water and Wastewater Treatment.* Vol. 3. 2004, New York: Iwa Publishing.

6. Clark, J.H. and D.J. Macquarrie, *Handbook of Green Chemistry and Technology.* 2002, Toronto: Wiley-Blackwell.

7. Lide, D.R., *CRC Handbook of Chemistry and Physics.* 1996.

8. USPeroxide. *How much does H2O2 cost.* 2009 [cited 2011 November]; Available from: http://h2o2.com/faqs/FaqDetail.aspx?fId=25.

9. Campos-Martin, J.M., G. Blanco-Brieva, and J.L.G. Fierro, *Hydrogen peroxide synthesis: An outlook beyond the anthraquinone process.* Angewandte Chemie-International Edition, 2006. **45**(42): p. 6962-6984.

10. Riedl, H.-J. and G. Pfleiderer, *Production of hydrogen peroxide.* Chemical Abstract, 1939. **33**(49337): p. 49337.

11. Oloman, C. and A.P. Watkinson, *Hydrogen-Peroxide Production In Trickle-Bed Electrochemical Reactors.* Journal of Applied Electrochemistry, 1979. **9**(1): p. 117-123.

12. Mathur, I. and R. Dawe, *Using On-Site-Produced Alkaline. Peroxide for Pulp Bleaching.* TAPPI Journal, 1999. **82**(3): p. 157-163.

13. Nozaki, M., *On-site Alkaline Peroxide Generation System.* TAPPI Journal, 1998. **52**(5): p. 616-622.

14. Oloman, C., *Electrochemical Processing for the Pulp and Paper Industry.* 1996, The Electrochemical Consultancy: Romsey, UK.

15.	Goldstein, J.R. and A.C.C. Tseung, *A Joint Pseudo-splitting/Peroxide Mechanism for Oxygen Reduction at Fuel Cell Cathodes.* Nature, 1969. **222**(5196): p. 869-870.

16.	Tryk, D.A., et al., *Fundamental Understanding of Electrode Processes in Memory of Professor Ernest B. Yeager.* The Electrochemical Society Proceedings, ed. J. Prakash, et al. 2005, Pennington, New Jersey.

17.	Davison, J.B., et al., *A Voltammetric Investigation of Oxygen Reduction in a Trickle Bed Cell Using Graphite Chip and RVC Cathodes.* Journal of The Electrochemical Society, 1983. **130**(7): p. 1497-1501.

18.	Yamada, N., et al., *Development of Trickle-Bed Electrolyzer for On-Site Electrochemical Production of Hydrogen Peroxide.* Journal of The Electrochemical Society, 1999. **146**(7): p. 2587-2591.

19.	Wiesener, K., et al., *N4 macrocycles as electrocatalysts for the cathodic reduction of oxygen.* Materials Chemistry and Physics, 1989. **22**(3–4): p. 457-475.

20.	Bouwkamp-Wijnoltz, A.L., et al., *Electrochemical reduction of oxygen: an alternative method to prepare active CoN4 catalysts.* Electrochimica Acta, 1999. **45**(3): p. 379-386.

21.	Yeager, E.B., *Dioxygen electrocatalysis: mechanisms in relation to catalyst structure.* Journal of Molecular Catalysis, 1986. **38**: p. 5-25.

22.	Bonakdarpour, A., et al., *Preparation and electrochemical studies of metal–carbon composite catalysts for small-scale electrosynthesis of H2O2.* Electrochimica Acta, 2011. **56**(25): p. 9074-9081.

23.	Xu, J., W. Huang, and R.L. McCreery, *Isotope and surface preparation effects on alkaline dioxygen reduction at carbon electrodes.* Journal of Electroanalytical Chemistry, 1996. **410**(2): p. 235-242.

24.	Gyenge, E.L. and C.W. Oloman, *Electrosynthesis of hydrogen peroxide in acidic solutions by mediated oxygen reduction in a three-phase (aqueous/organic/gaseous) system - Part II: Experiments in flow-by fixed-bed electrochemical cells with three-phase flow.* Journal of Applied Electrochemistry, 2003. **33**(8): p. 665-674.

25.	Gyenge, E.L. and W. Oloman, *Electrosynthesis of hydrogen peroxide in acidic solutions by mediated oxygen reduction in a three-phase (aqueous/organic/gaseous) system - Part I: Emulsion structure, electrode kinetics and batch electrolysis.* Journal of Applied Electrochemistry, 2003. **33**(8): p. 655-663.

26.	Forti, J.C., et al., *Electrochemical synthesis of hydrogen peroxide on oxygen-fed graphite/PTFE electrodes modified by 2-ethylanthraquinone.* Journal of Electroanalytical Chemistry, 2007. **601**(1-2): p. 63-67.

27.   Gao, M., et al., *Electrochemical characteristics and stability of poly(1,5-diaminoanthraquinone) in acidic aqueous solution.* Journal of Physical Chemistry C, 2007. **111**(46): p. 17268-17274.

28.   Gao, M., et al., *Effects of poly-1,5-diaminoanthraquinone morphology on oxygen reduction in acidic solution.* Electrochimica Acta, 2009. **54**(8): p. 2224-2228.

29.   Kullapere, M., et al., *Electroreduction of oxygen on glassy carbon electrodes modified with in situ generated anthraquinone diazonium cations.* Electrochimica Acta, 2009. **54**(7): p. 1961-1969.

30.   Lobyntseva, E., et al., *Electrochemical synthesis of hydrogen peroxide: Rotating disk electrode and fuel cell studies.* Electrochimica Acta, 2007. **52**(25): p. 7262-7269.

31.   Vaik, K., et al., *Oxygen reduction on phenanthrenequinone-modified glassy carbon electrodes in 0.1 M KOH.* Journal of Electroanalytical Chemistry, 2004. **564**(1-2): p. 159-166.

32.   Wilson, T., et al., *Anthraquinone-2-carboxylic-allyl ester as a new electrocatalyst for dioxygen reduction to produce H2O2.* International Journal of Electrochemical Science, 2006. **1**(Journal Article): p. 99-109.

33.   Yeh, S.Y. and C.M. Wang, *Anthraquinone-modified electrodes, preparations and characterizations.* Journal of Electroanalytical Chemistry, 2006. **592**(2): p. 131-138.

34.   Berchmans, S. and R. Vijayavalli, *Surface Modification of Glassy-Carbon by Riboflavin.* Langmuir, 1995. **11**(1): p. 286-290.

35.   Manisankar, P. and A. Gomathi, *Mediated oxygen reduction at a glassy carbon electrode modified with riboflavin and 9,10-anthraquinones.* Journal of Power Sources, 2005. **150**(Journal Article): p. 240-246.

36.   Manisankar, P., et al., *Riboflavin as an electron mediator catalyzing the electrochemical reduction of dioxygen with 1,4-naphthoquinones.* Journal of Electroanalytical Chemistry, 2004. **571**(1): p. 43-50.

37.   Wingard, L.B. and J.L. Gurecka, *Modification of Riboflavin for Coupling to Glassy-Carbon.* Journal of Molecular Catalysis, 1980. **9**(2): p. 209-217.

38.   Zagal, J.H., M.J. Aguirre, and M.A. Paez, *O-2 reduction kinetics on a graphite electrode modified with adsorbed vitamin B-12.* Journal of Electroanalytical Chemistry, 1997. **437**(1-2): p. 45-52.

39.   Bard, A.J. and L.R. Faulkner, *Electrochemical methods: fundamentals and applications*. 2 ed. 2001, New York: John Wiley & Sons.

40.   Cramer, C.J., *Essentials of Computational Chemistry: Theories and Models*. 2nd ed. 2004: Wiley.

41.   Young, D., *Computational Chemistry: A Practical Guide for Applying Techniques to Real World Problems*. 2001, New York: John Wiley & Sons, Inc.

42.   Ferreira-Aparicio, P., M.A. Folgado, and L. Daza, *High surface area graphite as alternative support for proton exchange membrane fuel cell catalysts.* Journal of Power Sources, 2009. **192**(1): p. 57-62.

43.   Klassen, N.V., D. Marchington, and H.C.E. McGowan, *H2o2 Determination by the I-3(-) Method and by Kmno4 Titration.* Analytical Chemistry, 1994. **66**(18): p. 2921-2925.

44.   Li, N., et al., *Experimental Study of Closed System in the Chlorine Dioxide-Iodide-Sulfuric Acid Reaction by UV-Vis Spectrophotometric Method.* International Journal of Analytical Chemistry, 2011. **2011**.

45.   Ovenston, T.C.J. and W.T. Rees, *The Spectrophotometric Determination of Small Amounts of Hydrogen Peroxide in Aqueous Solutions.* Analyst, 1950. **75**(889): p. 204-208.

46.   Anderson, R.J., D.J. Bendell, and P.W. Groundwater, *Organic Spectroscopic Analysis*. 2004, London: The Royal Society of Chemistry.

47.   Bunzler, H. and H. Gremlich, *IR Spectroscopy: An Introduction*. 2002, Weinheim, Germany: Wiley-VCH.

48.   Yadav, L.D.S., *Organic Spectroscopy*. 2005, Norwell, USA: Kluwer Academic Publishers.

49.   Schumb, W.F., C.N. Satterfield, and R.L. Wentworth, *Hydrogen peroxide.* Journal of the American Pharmaceutical Association, 1955. **45**(2): p. 128-128.

50.   Hossain, M.S., D. Tryk, and E. Yeager, *The electrochemistry of graphite and modified graphite surfaces: the reduction of O2.* Electrochimica Acta, 1989. **34**(12): p. 1733-1737.

51.   Schmidt, T.J. and H.A. Gasteiger, *Rotating Thin-film Method for Supported Catalysts*, in *Handbook of Fuel Cells: Fundamentals, Technology and Applications*, W. Vielstich, A. Lamm, and H.A. Gasteiger, Editors. 2003, Wiley: New York. p. 328.

52.   Castelain, M., et al., *Supramolecular assembly of graphene with functionalized poly(fluorene-alt-phenylene): the role of the anthraquinone pendant groups.* Chemical Communications, 2011. **47**(27): p. 7677-7679.

53.   Zhao, Y.H., M.H. Abraham, and A.M. Zissimos, *Fast calculation of van der Waals volume as a sum of atomic and bond contributions and its application to drug compounds.* Journal of Organic Chemistry, 2003. **68**(19): p. 7368-7373.

54.   Lee, H.B., A.H. Park, and C. Oloman, *Stability of hydorgen peroxide in sodium carbonate solutions.* TAPPI Journal, 2000. **8**(94).

Appendix A. Infrared Spectroscopy Band Assignment

Constitutional groups present in organic compounds are responsible for IR absorptions. Table A.1 lists some characteristic group frequencies, and provides a guideline for absorption band assignments. The absorption bands shift as a consequence of the environment in which the corresponding characteristic group is present. Hence assigning them becomes an assembly of puzzle pieces, and keeping the anticipated final picture in mind is necessary.

Complex organic molecules have a large number of vibrational modes, and each of which, involving a change in the molecular dipole moment, results in an IR absorption band. A typical IR spectrum may have hundreds of absorption bands, particularly in the fingerprint region (from about 1500 to 500 cm^{-1}). The primary objective of band assignment for the IR spectra in Fig. 4.2 in this context is to elucidate the synthesized RF-AQ is indeed an ester derivative of RF and CAQ. Therefore, we are particularly interested in bands that indicate the presence of ester and/or carboxylic acid groups. The many rich features in the fingerprint region are left unexplored.

As all of the studied organic compounds are highly conjugated, the broad bands around 3000 cm^{-1} are overwhelmed with stretching modes of the aromatics.

Fig. 4.2 a and b represents the spectra for the pure reagents, CAQ and RF respectively. Fig. 4.2a clearly shows adsorption bands characteristic of carboxylic acid. Most pronouncedly are the C=O stretch at 1700 cm^{-1}, the C-O stretch at 1280 cm^{-1}, and the O-H stretch at 935 cm^{-1}.

Fig. 4.2c shows strong evidence that the sample is a carboxylate ester, including the C=O stretch mode at 1730 cm^{-1}, and the two C-O stretch modes at 1240 and 1080 cm^{-1}.
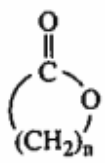
Table A.1 Characteristic infrared absorption frequencies (adapted from Yadav[48] with permission from Kluwer Academic Publishers)

Type	Group	Absorption frequency (cm^{-1})	Intensity*	Assignment and remarks
	CH_3—X	1441–1471	v	C—H asym. bending
	(X = F, Cl, Br, I)	1255–1475	v	C—H sym. bending
Aromatic compounds	Aromatic C—H	3000–3100	m	C—H stretch
	Aromatic C—C	1600±5	v	C=C skeletal stretch
		1580±5	m	Skeletal stretch; present when ring is further conjugated
		1500 ± 25	v	Skeletal stretch
		1450 ± 10	m	Skeletal stretch
	Monosubstituted benzenes	730–770	s	
		690–710	s	
	o-disubstituted benzenes	735–770	s	C—H out-of-plane bending
	m-disubstituted benzenes	750–810	s	
		680–725	$m{\rightarrow}s$	
	p-disubstituted benzenes	800–860	s	
	Aromatic C—H	1000–1300	w	In-plane C—H bending; usually difficult to assign because they are weak and C—O and other C—H bands occur in the same region
Alcohols and phenols	O—H	3590–3650	v	Free O—H stretch
		3200–3600	v	Intermolecular hydrogen bonded O—H stretch
		2500–3200	s	Intramolecular hydrogen bonded O—H stretch
	C—O	1000–1260	$m{\rightarrow}s$	C—O stretch
		~1050	s	C—O stretch primary alcohols
		~1100	s	C—O stretch secondary alcohols
		~1150	s	C—O stretch tertiary alcohols
		~1200	s	C—O stretch phenols
	O—H	1330–1420	s	In-plane O—H bending
		650–769	s	Out-of-plane O—H bending

Type	Group	Absorption frequency (cm^{-1})	Intensity*	Assignment and remarks
Ketones	R\C=O /R	1705–1725	s	C=O stretch; saturated, acyclic
		1680–1700	s	C=O stretch; aryl
		1660–1670	s	C=O stretch; diaryl
		1665–1685	s	C=O stretch; α,β-unsaturated, and $\alpha, \beta, \alpha', \beta'$ unsaturated, acyclic
		1705–1725	s	C=O stretch; six- and larger-membered ring
		1740–1750	s	C=O stretch; five-membered ring
		~1775	s	C=O stretch; four-membered ring
		1685–1705	s	C=O stretch; cyclopropyl
		1665–1685	s	C=O stretch; α,β-unsaturated cyclic, six- and larger-membered ring
		1708–1725	s	C=O stretch; five-membered ring
		1540–1640	s	C=O stretch; β-diketone, enolic
	o-amino- and o-hydroxy-aryl ketones	1635–1655	s	C=O stretch
	1,4- and 1,2-benzoquinones	1660–1690	s	C=O stretch
Carboxylic acids	—COOH	1700–1725	s	C=O stretch; saturated, aliphatic
		1690–1715	s	C=O stretch; α,β-unsaturated, aliphatic
		1680–1700	s	C=O stretch; aryl
		1720–1740	s	C=O stretch; α-halo
		1655–1665	s	C=O stretch; intramolecularly hydrogen-bonded
		2500–3000	m	O—H stretch; hydrogen-bonded, free O—H stretch, 3550 cm^{-1}

(Contd.)

Type	Group	Absorption frequency (cm^{-1})	Intensity*	Assignment and remarks
Carboxylate anions	—COO$^-$	1550–1650	s	C=O asym. stretch
		1300–1400	s	C=O sym. stretch
Esters	R—COOR′	1735–1750	s	C=O stretch; saturated acyclic
		1715–1730	s	C=O stretch; R = α,β-unsaturated or aryl group
		1750–1800	s	C=O stretch; R′ = α,β-unsaturated or aryl group
		1650	s	C=O stretch; β-ketoesters, enolic
		1000–1300	s	C—O—C sym. and asym. stretch; in all types of esters
Lactones (cyclic esters)	(cyclic structure: C=O with C—O and (CH₂)$_n$ ring)	1735–1750	s	C=O stretch; δ-lactone and larger rings, $n \geq 4$
		1760–1780	s	C=O stretch; γ-lactone, $n = 3$
		1820–1840	s	C=O stretch; β-lactone, $n = 2$
		1717–1730	s	C=O stretch; α,β-unsaturated δ-lactone
		1740–1770	s	C=O stretch; α,β-unsaturated γ-lactone
		~1800	s	C=O stretch; β,γ-unsaturated γ-lactone
Acid halides	—COCl	1790–1815	s	C=O stretch; fluorides higher, bromides and iodides successively lower
		1750–1800	s	C=O stretch; aryl and α,β-unsaturated
Acid anhydrides	—CO—O—CO—	1800–1850	s	C=O stretch; two bands
		1740–1790	s	
		1780–1830	s	C=O stretch; two bands, aryl and α,β-unsaturated, acyclic
		1710–1770	s	
		1820–1870	s	C=O stretch; two bands, saturated five-membered ring
		1750–1800	s	
		1780–1830	s	C=O stretch; two bands, aryl and α,β-unsaturated
		1710–1770	s	
		1050–1300	s	C—O stretching; one or two bands in all types of anhydrides

*s = strong, m = medium, w = weak, v = variable.
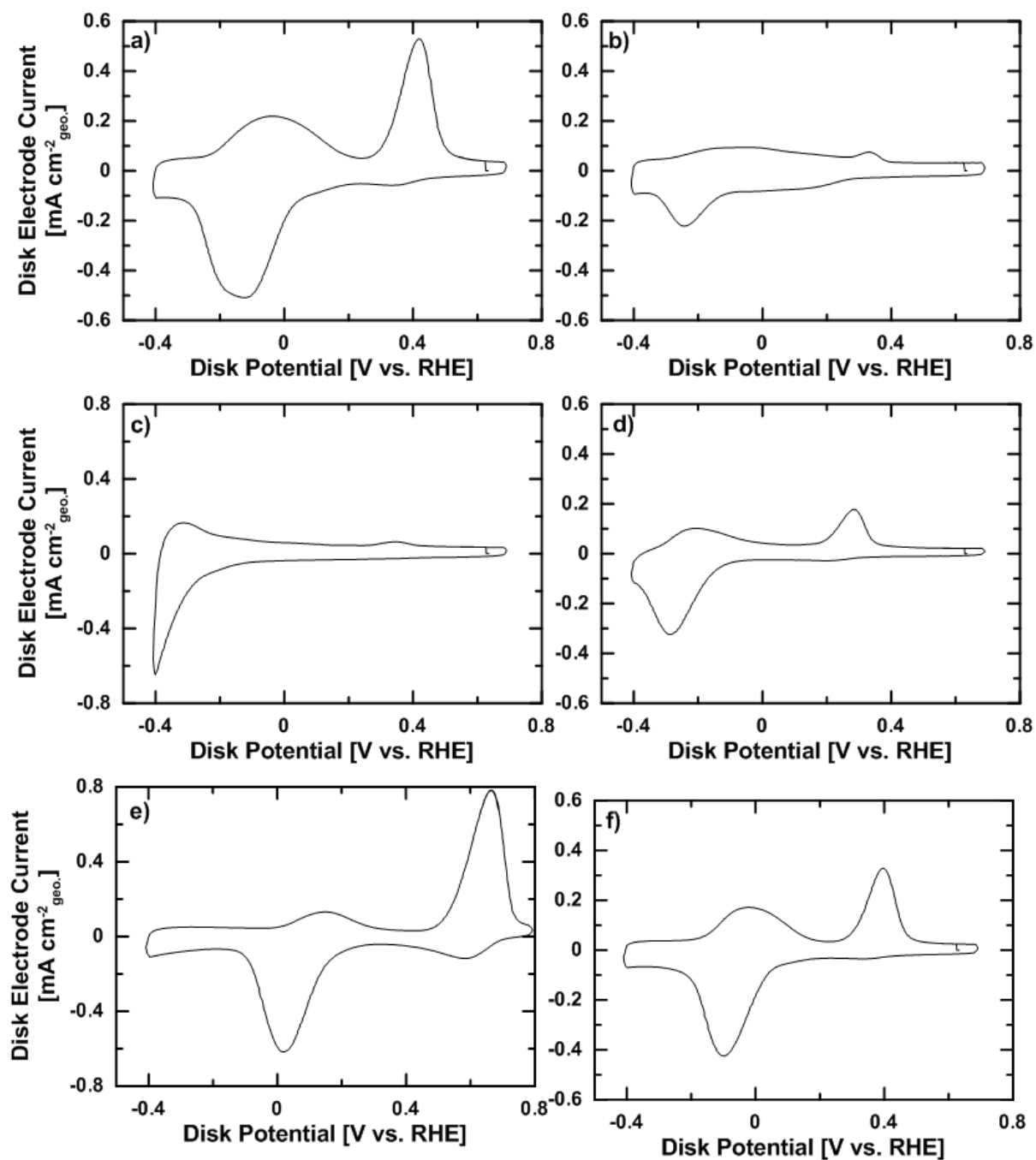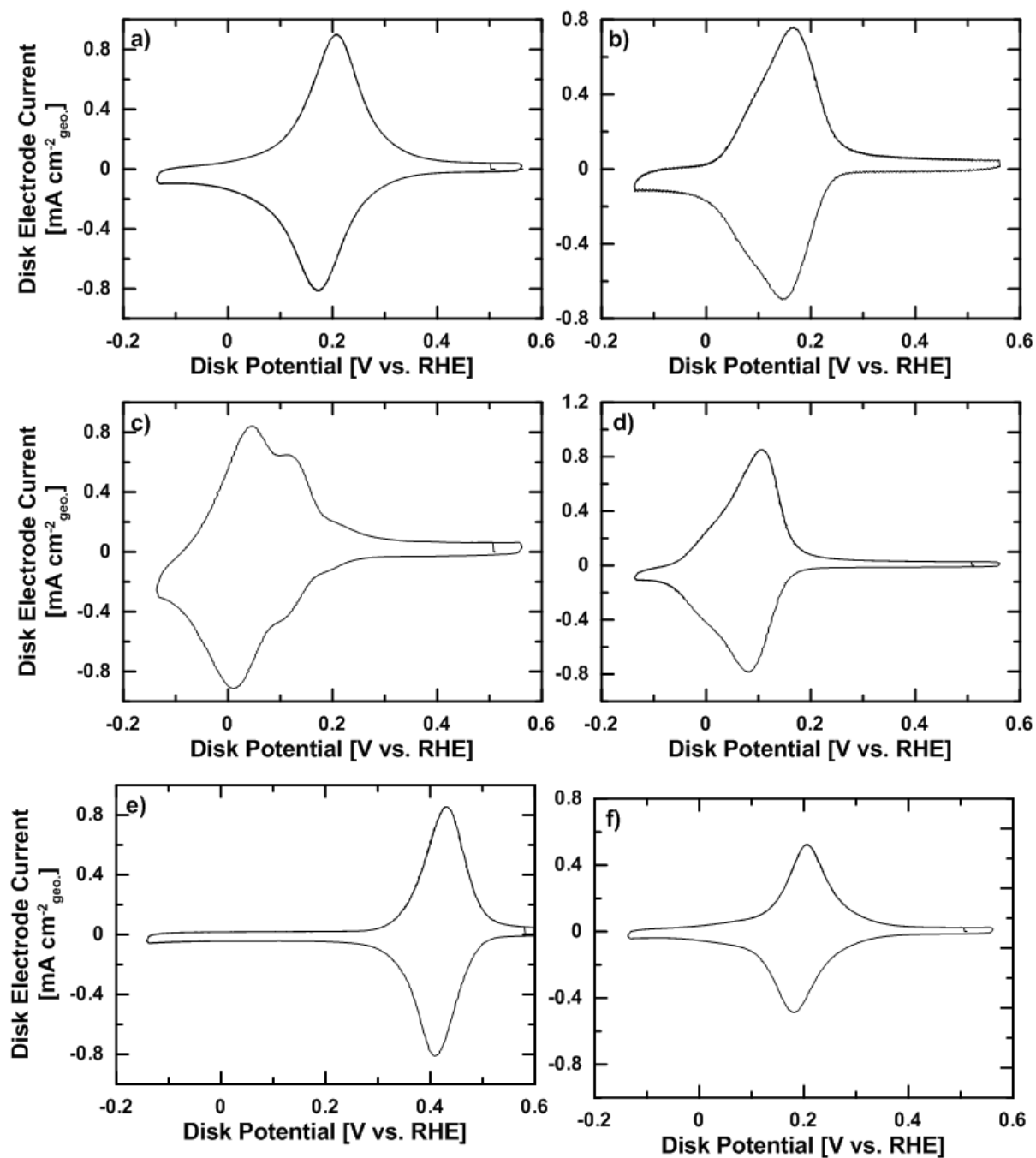
Appendix B. Cyclic Voltammograms

Figure B.1 Cyclic voltammograms for N_2 purged cells. (a) 10 wt% RF-AQ, (b) 10 wt% CAQ, (c) 10 wt% DAAQ, (d) 10 wt% EAQ, (e) 10 wt% PQ, and (f) 10 wt% RF. The experiments were performed using a catalyst loading of 0.66 mg cm-2 on the RRDE tip, 0.1 M K_2SO_4 electrolyte, at 21°C and 1 bar_{abs} pressure.

Figure B.2 Cyclic voltammograms for N_2 purged cells. (a) 10 wt% RF-AQ, (b) 10 wt% CAQ, (c) 10 wt% DAAQ, (d) 10 wt% EAQ, (e) 10 wt% PQ, and (f) 10 wt% RF. The experiments were performed using a catalyst loading of 0.66 mg cm-2 on the RRDE tip, 0.1 M H_2SO_4 electrolyte, at $21^{\circ}C$ and 1 bar_{abs} pressure.

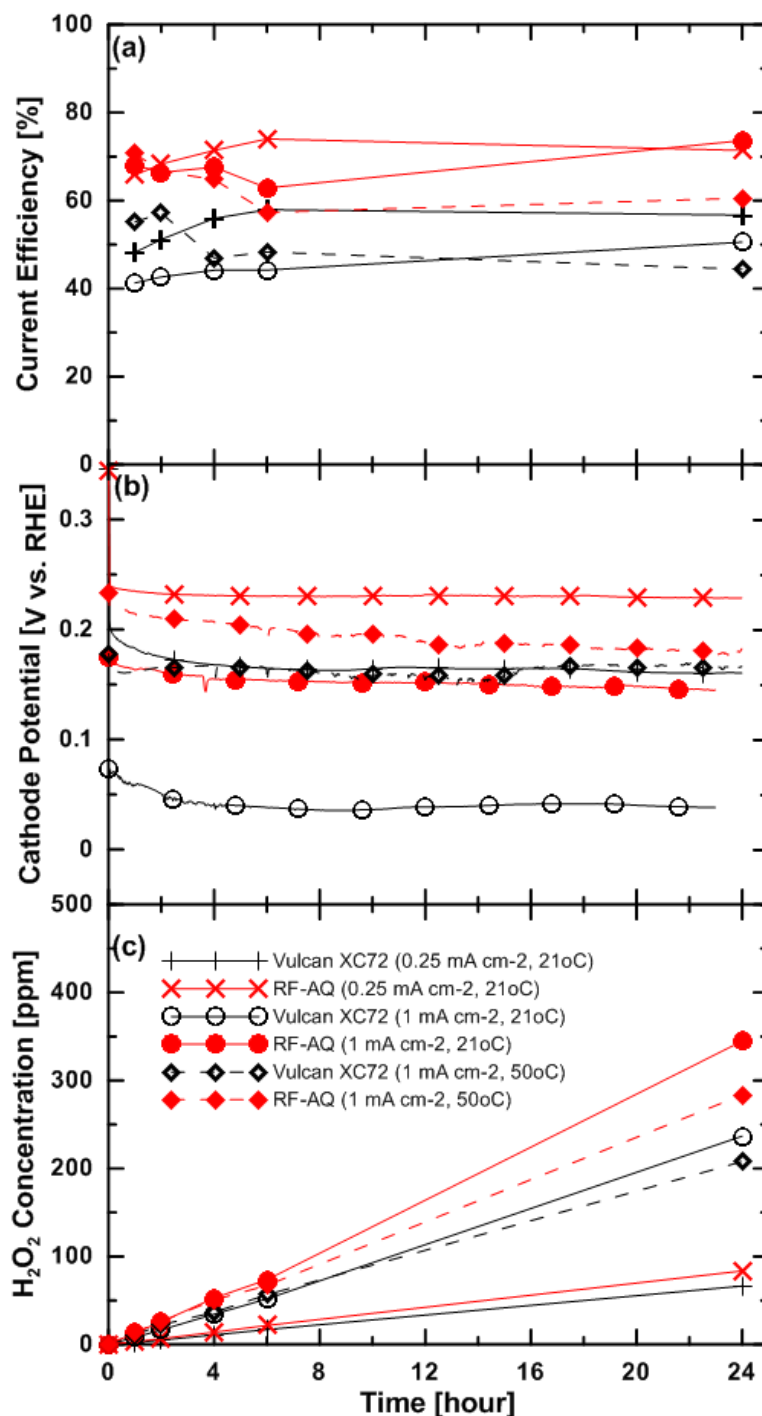# Appendix C. Chronopotentiometry

Figure C.1 Effect of the RF-AQ redox catalyst on H_2O_2 generation in a batch electrolysis cell. (a) Current efficiency of H_2O_2 generation. (b) Cathodic current density, and (c) H_2O_2 accumulative production normalized by the electrode surface area and H_2O_2 concentration as a function of time. The experiments were performed using RF-AQ 10 wt% on Vulcan XC72 carbon, 0.5 M H_2SO_4 electrolyte, using a composite catalyst loading of 2 mg cm^{-2}, at 1 bar$_{abs}$ pressure and 21°C or 50°C as specified.